# UNIVERSIDAD DE INVESTIGACIÓN DE TECNOLOGÍA EXPERIMENTAL YACHAY

**Escuela de Ciencias Físicas y Nanotecnología**

## TÍTULO: Cerium Doped Hydroxyapatite: Synthesis and Characterization

Trabajo de integración curricular presentado como
requisito para la obtención
del título de Ingeniero en Nanotecnología

**Autor:**

**Ponce Guzmán Juan Fernando**

**Tutor:**

Ph.D - **González Gema**

Urcuquí, junio 2023

**AUTORÍA**

Yo, **Ponce Guzmán Juan Fernando**, con cédula de identidad 1718644295, declaro que las ideas, juicios, valoraciones, interpretaciones, consultas bibliográficas, definiciones y conceptualizaciones expuestas en el presente trabajo; así cómo, los procedimientos y herramientas utilizadas en la investigación, son de absoluta responsabilidad de el/la autora (a) del trabajo de integración curricular. Así mismo, me acojo a los reglamentos internos de la Universidad de Investigación de Tecnología Experimental Yachay.

Urcuquí, junio 2023.

Firmado electrónicamente por:
JUAN FERNANDO PONCE GUZMAN

_____

Nombres y Apellidos
CI: 1718644295

**AUTORIZACIÓN DE PUBLICACIÓN**

Yo, **Ponce Guzmán Juan Fernando,** con cédula de identidad 1718644295, cedo a la Universidad de Investigación de Tecnología Experimental Yachay, los derechos de publicación de la presente obra, sin que deba haber un reconocimiento económico por este concepto. Declaro además que el texto del presente trabajo de titulación no podrá ser cedido a ninguna empresa editorial para su publicación u otros fines, sin contar previamente con la autorización escrita de la Universidad.

Asimismo, autorizo a la Universidad que realice la digitalización y publicación de este trabajo de integración curricular en el repositorio virtual, de conformidad a lo dispuesto en el Art. 144 de la Ley Orgánica de Educación Superior

Urcuquí, junio 2023.

Firmado electrónicamente por:
JUAN FERNANDO PONCE GUZMAN

Nombres y Apellidos
CI:1718644295

**Resumen**

Cristales de hidroxiapatita (HAp) e hidroxiapatita dopada con iones de ceria fueron sintetizados usando el metodo hidrotermal. Muestras que contenian seis diferentes concentraciones de ceria desde 0% hasta 25% fueron distribuidas en diferentes grupos que fueron sometidos a tratamientos de calor a 200 ºC, 400 ºC, 600ºC, y 800ºC para poder evaluar las propiedades del material resultante de CeHAp tomando en cuenta las condiciones mencionadas. Propiedades estructurales y morfologicas fueron analizadasa usando diferentes tecnicas de caracterización como Espectroscopia Infraroja de Transformada de Fourier (FTIR), Difracción de Rayos X (XRD), Espectroscopia de Raman, Microscopia de Electrones (SEM) y EDS. Además, para evaluar las propiedades ópticas del material, se uso Microscopia de Fluorescencia y espectroscopia UV-Vis. Spectra sugiera un intercambio exitoso entra los iones de Ca y Ce, los cuales a altas concentraciones y temperaturas siguieren un cambio un la estructura cristalina de la hidroxiapatite. el material muestra un gran potencial en el campo biomedico actuando como antibacterial y anti-inflamatorio debido a las propiedades obtenidas del ion de Ce con propiedades opticas mejoradas.

**Palabras Clave:**

Hidroxiapatita, Iones de ceria, Dopado, Propiedades, Tratamiento de Calor.

**Abstract**

Hydroxyapatite (HAp) and cerium ions doped hydroxyapatite (CeHAp) crystals were synthesized using the hydrothermal method. Six different cerium concentration samples from 0\% to 25\% were distributed in different batches which underwent heat treatment at 200 ºC, 400 ºC, 600ºC, and 800ºC in order to evaluate the properties of the resultant CeHAp material taking into account the conditions mentioned. Structure and morphology properties were analyzed using different characterization techniques as they are Fourier Transformed infrared spectroscopy (FTIR), X-ray powder diffraction (XRD), Raman spectroscopy, scanning electron microscopy (SEM), and energy dispersive X-ray spectroscopy (EDS). In addition, to evaluate the optical properties of the material, UV-Vis spectroscopy and fluorescence microscopy were employed. Spectra suggest a successful exchange of ions among Ca and Ce ions, which at high concentrations (>20\%) and at high temperatures (>600) suggest a change in the crystal structure of the hydroxyapatite. The material shows a great potential in the biomedical field acting as an antibacterial and anti-inflammatory material due to the properties obtained by the cerium ions, with enhanced optical properties.

**Key Words:**

Hydroxyapatite, Cerium ions, Doped, Properties, heat treatment.

# Abstract

Hydroxyapatite (HAp) and cerium ions doped hydroxyapatite (CeHAp) crystals were synthesized using the hydrothermal method. Six different cerium concentration samples from 0% to 25% were distributed in different batches which underwent heat treatment at 200 ºC, 400 ºC, 600ºC, and 800ºC in order to evaluate the properties of the resultant CeHAp material taking into account the conditions mentioned. Structure and morphology properties were analyzed using using different characterization techniques as they are Fourier Transformed infrared spectroscopy (FTIR), X-ray powder diffraction (XRD), Raman spectroscopy, scanning electron microscopy (SEM), and energy dispersice X-ray spextroscopy (EDS). In addition, to evaluate the optical properties of the material, UV-Vis spectroscopy and fluorescence microscopy were employed. Spectra suggest a successful exchange of ions among Ca and Ce ions, which at high concentrations (>20%) and at high temperatures (>600) suggest a change in the crystal structure of the hydroxyapatite. The material shows a great potential in the biomedical field acting as an antibacterial and anti-inflammatory material due to the properties obtained by the cerium ions, with enhanced optical properties.



**Keywords:** Hydroxyapatite, Cerium ions, Doped, Properties, heat treatment.

# Acknowledgements

I would like to express my sincere gratitude to all my professors for the knowledge and values provided during this journey, mostly to my advisor Dr. Gema Gonzalez and co-advisor Dr. Sarah Briceño who has given me the proper guidance with their experience and skills besides its predisposition to all kind of help in order to succeed in this project. Also, to my incredible family, especially my mother Gabriela, my father Marco Vinicio, my sister Doménica and my loving pet Tyson who held my spirit during this process.

# Contents

# List of Figures

# List of Tables

# Chapter 1

# Introduction

With the convergence of nanotechnology and medicine fields, an increasing interest of researchers nowadays is focusing on the so-called "emerging" world of nanomedicine. The first person to popularize the term as the new healthcare approach was Robert Freitas [12] in 1999, over 20 years ago, with futuristic promises on the development of the field [13]. Nevertheless, up to 2004, only 72 articles were published, according to Medline, but during the decade after (2005-2015), the number of related works exponentially grew to over 10.500 [14]. As nanotechnology can be understood as an atom-by-atom approach in the fabrication of nanodevices, nanomedicine is seen as a cell-by-cell approach of human diseases. Nanomedicine can be summed up as the application of a large self-assembling number nanometric-medical tools that performs successful parallel-process disease at the level of million cells symultaneously [13]. Hydroxyapatite is a candidate to be used in the development of new materials applicable to human welfare. HAp is the most abundant inorganic compound in our body as it is the principal component of bone and teeth structure. HAp is commonly arranged in an hexagonal structure P63/m space group with characteristic flexibility that can accept a great variation of substitutions that can lead for example in functional groups as $OH^-$ and $PO_[4]^{3+}$ to be substituted for $CO_3^{2-}$ resulting in carbonated forms of apatite or ionic substitutions among the $Ca^{2+}$ with mono, bi, tri, tethra and even hexa-valent ions that comprise almost the fifty percentage of the periodic table. Mechanical, biological and antibacterial properties had been reported to be enhanced by added ions like the $Ag^{3+}$. Rare earth elements could also provide some of the mentioned characteristic as well as optical improvement through fluorescent responses proper of the lanthanide nanoparticles [15 16 17]. Particularly, substitutions of cerium ions into the apatite structure, started to gain interest due to the due to nano-compounds proven antibacterial and luminescent capabilities. $CO_2$ has been reported as a probing agents for fluorescent imaging and biosensors due to its excellent response under ultraviolet (UV) excitation [18 19 18]. HAp and substituted HAp displays promising, potentially human healthcare applicable, characteristics that could be used as biological probing, luminescent probing, antibacterial reagents, scaffold tissue engineering or for drug delivery systems [20 17 15]. For the purpose of this work, it is taken into consideration that substitution and doping are two different processes that can occur when introducing foreign ions into a material. Substitution involves the exchange of ions with similar ionic radii and charges, resulting in minimal changes to the crystal structure and properties of the material. On the other hand, doping involves intentionally

introducing foreign ions result in significant changes to the crystal structure and properties of the material, in this case the substitution of Ce ions for Ca ions in the HAp crystal structure is what initially occurs. However, as the concentration of Ce ions increases, it begins to act as a dopant, causing structural changes and altering the properties of the material.

For the present work, a hydrothermal route synthesis was carried out in order to obtain pure nanocrystals of hydroxyapatite and cerium ions substituted form of the hydroxylated apatite to analyze the structural and optical effects of the dopant that as the concentration is varied and submitted to different heat treatments of 200 ºC, 400 ºC, 600 ºC, and 800 ºC. Few reports exist on the optical and fluorescent nature of hydroxyapatite substituted with cerium as a novel biomaterial. Nevertheless, a study between the concentration of Ce nanoparticles and the temperature effect in the apatite has not been done as of the authors knowledge

## 1.1 Problem Statement

Over the years increasing efforts in assure human welfare has lead into the need for new biomedical materials with enhanced properties such as antibacterial, anti-inflammatory and optical capabilities. Cerium doped hydroxyapatite has the potential to meet these needs, making it an important material for biomedical applications.

## 1.2 General and Specific Objectives

To synthesize hydroxyapatite nanocrystals doped with cerium ions for obtaining a novel material as a candidate for biomedical applications as antibacterial, anti-inflammatory, UV protector or imaging while perform a detailed structural characterization.

## 1.3 Specific Objectives

1. Synthesize doped and raw hydroxyapatite particles through Hydrothermal method varying the Ce concentration and temperature of calcination.
2. Study the morphological, structural and optical effects of the substituted ions in the HAp host using FTIR, XRD, Raman, SEM, EDS, UV-vis spectroscopy.
3. Gather the resulting information in order to relate the results and understand the changes obtained with the substitution.

# Chapter 2

# Theoretical Background

## 2.1 Hydroxyapatite

Hydroxyapatite (HAp) is a type of calcium-phosphate (CaP) based bio-ceramic with chemical formula $Ca_{10}(PO_4)_6(OH)_2$ [21]. HAp constitutes 65% of the mineral fraction of human bones and the predominant mineral in dentine and tooth enamel structure. [22]. This hydroxylated form of apatite is the most stable of the CaP family at relatively normal temperatures and with a pH level higher than 4.2 [21]. Hydroxyapatite has an atomic Ca/P ratio of 1.67, with 39% by weight of Ca, 18.5% of P and 3.38% of OH [23]. The HAp derived from natural sources or synthetic sources is regarded as a bioactive substance since it forms a strong chemical bond with host bone tissue. Hence it is recognized as a suitable bone graft material. HAp is not only bioactive but also osteoconductive, non-toxic, and non-immunogenic, and its structure is crystallographically similar to that of bone mineral with an adequate amount of carbonate substitution [24].

### 2.1.1 Crystalline structure

Chemically pure HAp crystallizes in the monoclinic space group $P2_1/b$ [25]. However, at temperatures above 250 °C, there is a monoclinic-to-hexagonal phase transition to HAp with a space group $P6_3/m$. [26]. The structure of hexagonal HAp is illustrated in Figure 2.1. In this structure, the calcium ions can occupy two sites I and II. Calcium I sites are on the trigonal axis of the structure at (1/4, 3/4, 1/2 and 3/4, 1/4, and 1/2 positions). The Ca II ions form equilateral triangles at z = 1/4 and z = 3/4, on the 63-axis of the structure. These ions constitute part of the walls of 'channels' where the monovalent sites are located. They correspond to the narrowest part of the channels with a diameter of 0.27 nm for CaP apatites. At z = 1/2, the channels appear slightly larger (0.29 nm), and they are limited by a distorted hexagon of oxygens belonging to $PO^{3-}_4$ anions.

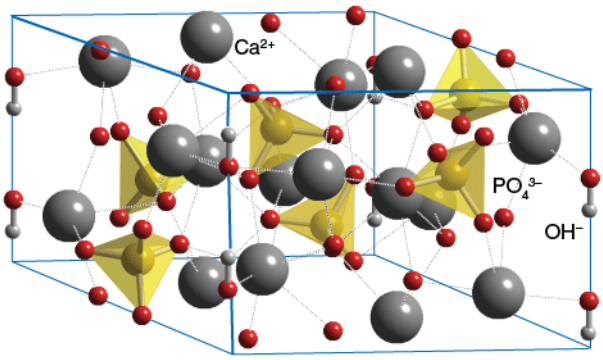


Figure 2.1: Hydroxyapatite crystal structure. Obtained from Deshpande, et al [1]

Owing to the existence of these channels, apatites have sometimes been compared to zeolites; the channels appear smaller than those generally found in zeolites, and they are mono-dimensional and obstructed by ions, which considerably limit the exchanges at low temperatures and the trapping of molecules [26].

### 2.1.2 Synthesis of Hydroxyapatite

Several method are reported to obtain hydroxyapatite, which can be classified into distinct groups depending on the properties that the material will display. *Dry methods* such as Solid-state reactions or mechanochemical procedures can be performed. These methods can obtain samples with various morphology, low purity, and various particle size [27 28]. *Wet methods* like chemical precipitation, hydrolysis, and sol-gel produce various morphology with variable purity except for the hydrolysis method which is related to high purity [29]. Particle size varies as the first wet method creates most nanosized particles; hydrolysis is set for variable size meanwhile Sol-Gel produces nanoparticles [30]. *Hydrothermal methods* include emulsion and sonochemical types, which provide mostly spherical and needle-like as well as miscellaneous morphology [31]. Methods are reported as having high purity with nanoparticle size [32 33]. Other methods disclosed are *high* temperature like combustion and pyrolysis. For the first method, Kaygili, et al [34] described mostly nanosized particles with various morphology, high purity, and mostly nanosized particles. For pyrolysis, Cho, et al [35] recorded miscellaneous morphology depending on the initial concentration of the precursor solution as well as variable purity and nano-to-micron particle size development. Hydroxyapatite can also be obtained through biogenic sources, showing different morphology, high quality, and variable particle size [36 37]. In addition, there can be a combination of methods that may lead mostly nanosized particle sizes with variable purity and morphology [38 39].

### 2.1.3 Hydroxyapatite substitution mechanism

Hydroxyapatite structure allows large variations from its theoretical composition and the formation of non-stoichiometric forms and ionic substitutions. More than half of naturally occurring elements can be significantly accommodated in the apatite lattice. Some of the substitutions can only be carried out during the synthesis process. Meanwhile, a limited ion exchange between solid form apatite and certain surrounding solution can also take place [40]. HAp

structure, as described above, is composed of hexagonal $Ca^{2+}$ and $(PO_4)^{3-}$ arrangements on $OH^-$ columns that allow the incorporation of a wide range of different ionic substitutions of calcium [21]. Several reports describes the monovalent ($Na^+$, $K^+$), divalent ($Ba^{2+}$, $Cd^{2+}$, $Mg^{2+}$, $Mn^{2+}$, $Pb^{2+}$, $Sr^{2+}$, etc.), trivalent ($Al^{3+}$, $Cr^{3+}$, $Fe^{3+}$, rare earths ions $REE^{3+}$, etc.), tetravalent ($Th^{4+}$, $Ti^{4+}$, $U^{4+}$) or even hexavalent cations ($U^{6+}$ that can take place in the Ca sites in the hydroxyapatite structures [41]. $OH^-$ and $(PO^4)^{3-}$ groups by some anionic groups such as $Cl^-$, $F^-$, $(CO_3)^{2-}$ and $(VO_4)^{3-}$ [21]. With the anionic or cationic type of substitution variation, HAp structural properties are altered, causing changes in their physical-chemical and biological properties. Such substitutions are accompanied by changes in network parameters and unit cell volume, which are generally related to the size of the cation ionic radius compared to that of $Ca^{2+}$ [21]. The incorporation of foreign cations may affect properties like morphology, lattice parameters, surface characteristic, solubility, and mechanical and biological properties of HAp biomaterials [40]. However, it became clear during synthetic studies that predicting the composition of compounds with apatite-type structures could not be done solely based on satisfying the valence considerations because the occurrence of the apatite-type structure appears to be determined by the ratio of the mean size of "A" ions (i.e. Ca ions in fluorapatite or hydroxyapatite) to the mean size of "X" ions in $XO_4$ [42] [43].

## 2.2 Ceria nanoparticles

Cerium oxide, also called ceria, is a promising technological ceramic material with wide band gap (3.15 eV) and a dielectric constant of 24.5 [44]. Although, band gap value can vary due to the particle size, morphology and defects. Ceria presents a yellow appearance and crystallizes in the cubic fluorite crystal structure, containing a space group Fm3m in which $Ce^{4+}$ ions are surrounded by 8 equivalent $O^{2-}$ ions forming the corner of a cube, with each oxygen ion coordinated to the cerium ions as shown in figure 2,2 [1] [45]. Ceria undergo structural changes with the conversion process of $Ce^{4+}$ ions to $Ce^{3+}$ ions due to the increase in formation rate of oxygen vacancies produced by the increase in temperature [46].

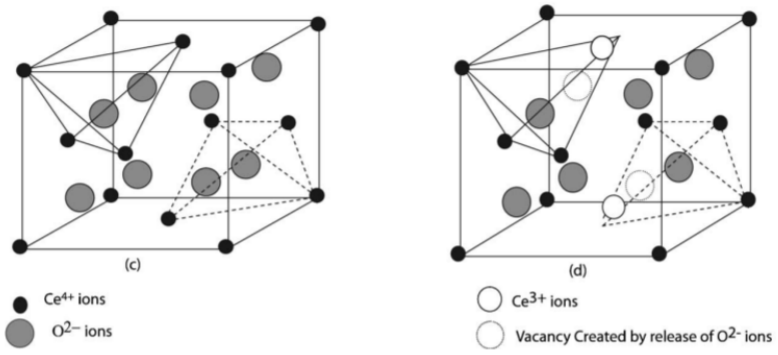


Figure 2.2: Distorted crystal structure of nanoceria due to oxygen vacancy creation and replacement of Ce4+ ions by Ce3+ ions by Deshpande et al. [1]

By the presence of intrinsic defects, coordination number between cerium ions and oxygen ions change from eight to seven by this increase in temperature, which introduces $Ce^{3+}$ ions into the crystal lattice as 2 electrons from an oxygen atom are transferred to two cerium neighboring ions, which leaves the unit cell, forming a vacancy site (figure 2.2). Cerium ions are reduced from the $Ce^{4+}$ state to $Ce^{3+}$ that produces a form of $Ce^{3+}$ ion with Ce $4f^1$ configuration. The increasing interest for this material has increased as it can be applied to various biomedical applications such as gas sensors, fuel cells, polishing materials, phosphors, energy storage materials, or catalysts. Another significant uses that ceria can offer relies on UV absorbents[47], ideally for sun protection, as well as several studies suggest the ability of ceria nanoparticles to mitigate oxidative stresses and reactive oxygen species (ROS) at a biological level[48]. This material can also act as an scavenger for free radicals excess such as peroxide ($O^{2-}$), and hydroxyl radical ($OH^-$), which plays a key role at damaging the molecular structures in biological organisms and stripping electrons from cellular macromolecules[46]. Several methods have been developed to prepare Ceria particles, including conventional hydro-thermal, co-precipitation, polymeric precursor, flow method, organo-metallic decomposition, and microwave-assisted heating[49].

## 2.3 Luminescence

Luminescence refers to the emission of light from an excited electronic state of a molecular species. In luminescence, some energy source kicks an electron of an atom out of its lowest energy state into a higher-energy state (excited). The electron gives back the energy in the form of light in the visible region so that it can return to its original ground state. This emitted wavelength corresponds to a characteristic of the luminescent material and not due to the incidence radiation. This type of "cold" emission, which does not include black body radiation, involves two steps: (1) The excitation of the electronic system of a solid material to a higher energy state, and (2) the subsequent emission of photons[50]. Figure 2.3 shows a Jablonski diagram of the energy levels of an hypothetical atom.

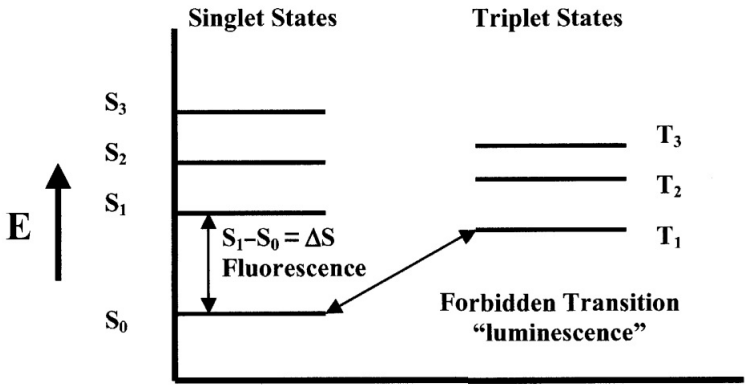


Figure 2.3: Jablonski diagram showing the energy levels of a hypothetical atom. Retrieved from Wolf, David[2]

Light emission takes place at a specific time "$\tau_c$" after the absorption of the initial radiation; this parameter allows the luminescence phenomena to be classified into fluorescence where the value is in the range of $\tau_c<10^{-8}$ s and an independent temperature process is carried out[50]. Meanwhile, phosphorescence occurs when $\tau_c>10^{-8}$ where the process involves temperature. In addition, phosphorescence phenomena can be further divided into two divisions, a short period where $\tau_c<10^{-4}$ s and a long period where $\tau_c>10^{-4}$ s which is called Thermo-luminescence. Several varieties of luminescence types exist depending on the source used in order to trigger the energy of the luminescence, i.e. the emission of light is produced by the release of energy from a chemical reaction takes the name of *Chemi-luminescence* and if the resulting emission is generated in response to an applied electric field, this type of luminescence is known as *Electro-luminescence*[50].

### 2.3.1 Photoluminescence

Emitted resulting light due to the excitation of electromagnetic radiation i.e. photons, is known as *Photoluminescence*. It is a less specific term that embraces both fluorescence and phosphorescence. Photoluminescence has a broad application area, from whitening substances in washing powder to plasma screens for large-scale displays. A particular type of luminescence has a very slow decay, with the emission continuing for minutes or hours. This type of luminescence is called long-lasting or persistent luminescence and is commonly used in road safety and exit marking. After the absorption of a photon induces a transition to an excited electronic state, the material relaxes radiatively (spontaneous emission), non-radiatively (thermal relaxation), or through both routes. (cite Lumi book).

## 2.4 Hydroxyapatite Photoluminescence

Intense self-activated photoluminescence (PL) processes are expected in HA samples due to high structural and superficial detect densities[51]. As a promising luminescent bio-material, some studies have been developed to understand the process for the given response of Hydroxyapatite fully. The PL of HAp depends on the defect energy level formation, structure, and size of the nanoparticle.

### 2.4.1 Structural and Surface Defects-related Response

As referred with anteriority stoichiometric hydroxyapatite , chemically formulated as $Ca_{10}(PO_4)_6(OH)_2$ with phosphate clusters ($PO_4$), typically forming a hexagonal crystal pattern that is described by space group $P6_3/m$. Ca species are not located in the same crystallographic sites in this structure, and the corresponding general formula of SHA is $Ca(1)_4Ca(2)_6(PO_4)_6(OH)_2$. Ca(1) sites form columns on the ternary axes which are surrounded by nine oxygen atoms of PO4 tetrahedra obtaining $CaO_9$ clusters. Ca(2) sites are located at the corners of equilateral triangles forming the hexagonal channels of the structure. these species are surrounded by six O atoms that consist of the $[PO_4]$ clusters and one OH group inside the channel, resulting to $[CaO_7H]$ clusters. The hexagonal character of the HA lattice can be retained, even in the presence of various ionic substitutions and vacancies[52 53 54]. According to Machado, et al[3]. these vacancies in HAp lead to changes in the electronic structure and density of e– h pairs which, in turn, may affect

the intrinsic PL emission. These defects promoted the formation of additional energy levels within the band gap, are possibly responsible for the HA´s luminescent properties. Figure 2.4 represents a general model proposed for the mechanism of luminescence. Factors that favor the defect formation in solid matrices are variable depending on the synthesis and processing technique. Experimental parameters such as temperature, pressure, reaction medium, sample type, etc. also induces defect formation[55].

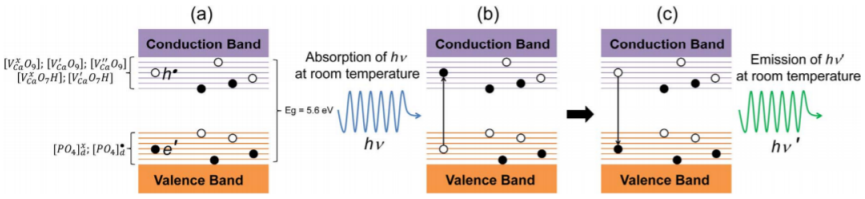


Figure 2.4: (a) Schematic of band structures of HAp (b) excitation process (formation of e-h• pairs); (c) recombination processes of e-h• pairs, which may result in PL emission. Taken from Machado, et al[3].

The effect of carbonates on hydroxyapatite in the photoluminescence response studied by Gonzalez et al. in different samples synthesized by chemical precipitation results in a luminescent effect dependent on carbonates impurities and $OH^-$ content. HAp samples were calcined to active the presence of defects and impurities thermally with the samples, figure 2.5 describes a schematic model proposed by Gonzalez, et al. Some responses were higher than others for the different samples depending on the synthesizing process of each, as in correlation with Machado. The luminescent behavior was ascribed to the recombination of defects between energy levels within the band gap[4].

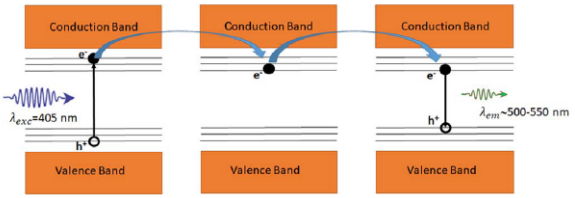


Figure 2.5: Schematic Model Proposed for PL emission of Hydroxyapatite under a excitation at λ= 405 nm, contribution of defective energy levels within the band gap. Taken from Gonzalez, et al[4]

### 2.4.2 Substitution Luminescent effects

Material interaction with light leads to transmission, absorption, and reflection that depends on refractive index, wavelength, dielectric constant, and dopants. The substitution of Ca in the hydroxyapatite structure can play a vital role creating abundant defects or vacancies in the lattice of the specimens. Either transmittance or reflectance is expected when the bound charges of the material are exposed to light. Depending on the substituting material, different phases and structures of the HAp may be possible[56]. HAp band gap varies due to the formation of many

defects in energy levels in between valence and conduction bands in presence of dopants. Some excited electrons are recombined with holes promptly to produce radiative emission. nevertheless, the emission might be non-radiative as well. New hostages can create either active light or inactive centers of emission at different wavelengths. However, it also depends on the excitation wavelength as well. In order to reduce non-radiative emission, the doping concentration must be properly tuned to elude the creation of concentration quenching; otherwise, centers of non-radiative are facilitated[57].

## 2.5 State of the Art

### 2.5.1 Hydroxyapatite doped systems

Optical as well as photoluminescence effects of HAp can be affected due to dopant addition into the structure. HAp allows is able to host distinct ions into its crystalline structure as of its apatite nature that possesses two non-equivalent sites, which can be described with cations labeled M (I) and M (II)[21]. This unique structure is responsible in the formation of solid solutions and acceptance of substitutions. The presence of phosphate ions supports the emission of photons of different wavelengths. Metal ions addition in the lattice of HAp adjusts the defect energy levels while changing the chemical potential[57]. The doped HAp helps the trapping of photons at defect sites or eases transmission, allowing the materials to become an option for optoelectronic device applications. These properties are dependant of the absorption, transmission, and band gap[57]. Several emissions are possible due to the formation of defect energy levels coupled with the HAp energy levels, which alters the rate of recombination of electron and hole pairs. Further, the doping concentration varies the active centers of recombination. Popa and Ciobanu[58] reported an enhanced PL due to the cerium ions doped HAp without any structural change, Ammar, et al reported that the band gap of erbium-doped HAp was reduced, displaying red and green emissions[59]. Feng et al[60]. reported that the Eu3+/Gd3+ dual-doped nanorods of HAp show enhanced PL with sustained ibuprofen (IBU) release. One dimensional nanostructures as zero dimension significantly affect the electronic motion establishing various energy levels due to the quantum confinement effect. When light is directed torwards the materials, various local emissions come about, which are absorbed in the matrix, and leading to partial photons emission. Optical responses, band gap, as well as emission behavior of materials may on thermal treatments. Thermal defects and production of active centers were assumed as responsible of the recombination rate at slow or rapid way of the electron and hole pairs[57].

### 2.5.2 Substitution with rare earth elements

Rare earth elements (REEs) have attracted attention in the past decade due to their several applications as magnets, catalysts, electronics, alloys, ceramics, etc. REEs are important in new technologies, such as LCD (liquid-crystal display), batteries, catalytic converters, and green technologies. Lanthanide-doped nanoparticles are being studied as a newly emerging type of luminescent optical label that could represent an alternative to the organic fluorophores and quantum dots used in the biomedical field, considering their great quantum yield, considerable Stokes shift, enlarged lifetime, and great stability[15]. Lanthanide ions have photo-luminescent properties in the visible and near-infrared

regions, principally when they are joined with phosphate compounds such as apatite[61]. Moreover, luminescent properties could be induced into hydroxyapatite by replacing the calcium ($Ca^{2+}$) ions with different luminescent rare-earth elements[40]. HAp doped nanoparticles may serve as a notable candidate for biological imaging and drug delivery. Previous investigations had proposed CaP nanoparticles as fluorescent probes following rare earth elements doping. Therefore, HAp could exhibit fluorescence under visible lights if it is doped with foreign fluorescent ions, from which $Eu^{3+}$[62] and $Tb^{3+}$[63] are the most intense emitting elements. Despite this, the size of particles and/or the fluorescent radiation in the cells cannot be very well supervised, which is a limitation in the functionality of these materials. Rare earth elements (REEs) are the term frequently used for the elements from lanthanum to lutetium (Z numbers 57–71).

### 2.5.3 Hydroxyapatite substitute with cerium

Nowadays, the interest in cerium nanoparticles has increased due to the properties this lanthanide can enhance and provide to a HAp system. Feng et al. synthesized cerium-substituted HAp using a hydrothermal method studying the concentration variation (up to 10% wt.) of the $Ce^{3+}$ ions that led to a morphology change from short rods to needle shape as this parameter increased[60]. Lin et al. using the sol-gel method, obtained a successful substitution of $Ce^{3+}$ and Ca and in the same way the morphology was modified from rod-shape to needle shape. Nevertheless, it was found that antibacterial properties could be displayed[64]. Heading into the last decade, Ciobanu et al. started the way for the exploration of the effects that the other form of cerium ($Ce^{4+}$) shows. The group reported single-phased Ce-substituted nanoparticles with irregular sizes, mostly from 20 nm to 60 nm, with increased antibacterial properties. Phatai et al. presented antithetical results as secondary phases such as $\vartheta$-tricalcium phosphate and calcium oxide along with the HAp phase using ultrasonic assisted sol-gel technique[65].

In the last three-year period, the interest in cerium (IV) grew. Padmanabhan et al.[66] reported another sol-gel method to obtain transformed Ce-HAp with similar hardness exhibited by bones, significant antibacterial effect, and a notable drug release profile. Drug delivery applications were described by Singh et al. in Ce-HAp mesoporous nanorods with a 43% enhancement in drug load compared to pure HAp samples under microwave synthesis[67]. Lastly, Paduraru et al. used a co-precipitation method in order to perform a cytotoxicity and biocompatibility evaluation resulting in a nontoxic specimen with improved biological properties that, with its fluorescence properties, can act as luminescent labeling materials[68].

### 2.5.4 Co-doped Hydroxyapatite systems

Co-doped Hydroxyapatite systems research field has been increasing as showing enhancing results on the HAp mechanical, biological, and optical properties depending on the added element. Xie, et al[69] has performed a work where HAp nanocrystals co-doped with $Eu^{+3}$/$Gd^{+3}$ where biocompatible, biodegradable and luminescence is enhanced with the potential to act as a fluorescent imaging agent *in vitro* and in vivo

## 2.6 Experimental Characterization Techniques

### 2.6.1 Photoluminescence spectroscopy

Photoluminescence (PL) spectroscopy provides a non-contact and nondestructive technique for material characterization in the scientific research. PL is described as a quantum mechanical process in which a photon is absorbed into a material by transferring its energy to an electron in the ground state and exciting it to an excited state within the femtosecond timescale[70]. When there are multiple excited states as in organic molecules, electrons are excited to a higher excited state, and rapidly relax in a non-radiatively way to the lowest excited states by exciting molecular vibrations in molecules or emitting phonons in solids in pico-second order, which is called thermalization or more precisely denoted internal conversion occurring between the states of the same spin multiplicity[71]. Subsequently, the electrons recombine radiatively to the ground state by emitting photons, which is called PL. Radiative transitions during thermalization are difficult and rarely happen; they are called hot luminescence. Thus, the absorbed photons are usually higher in energy than the emitted photons; this energy is called the Stokes' shift. One should note that besides the absorption, part of the incident light is reflected and another part is scattered. The scattering is divided into two types: Rayleigh scattering, which is elastic without annihilation or creation of excitations as phonons, and Raman scattering, which is inelastic and accompanied by annihilation or creation of phonons[70]. Figure 2.6 shows a schematic photoluminescence arrangement.

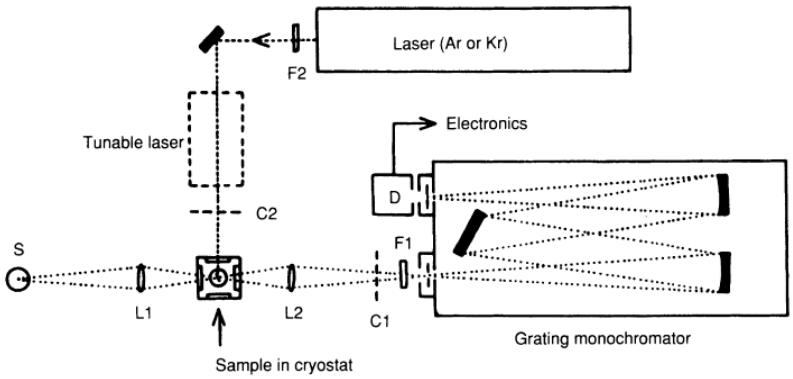


Figure 2.6: Photoluminescence arrangement, with laser, sample and cryostat, monochromator, and detector (D). Lens L2 focuses the PL signal; filters Fl and F2 block unwanted laser light; chopper CI modulates the light for lock-in detection. (The same arrangement serves for Raman spectroscopy, with the single-grating monochromator replaced by a double unit.) The tunable laser and chopper C2 are used for photoluminescence excitation (PLE) spectroscopy. Lamp S and lens L I are used for absorption spectroscopy[5]

### 2.6.2 Raman Spectroscopy

Raman spectroscopy is a branch of vibrational spectroscopy, which allows a relatively easy interpretation as a highly sensitive structural identification of trace amounts of chemicals based on their unique vibrational characteristics or fingerprints[6]. Figure 2.7 shows a schematic form of Raman spectroscopy. It measures the shift in frequency of inelastically scattered light from the sample when the photon from incident light strikes a sample molecule and produces a scattered photon. When the outcoming scattered light is a photon with a lower frequency value than the original photon, it is described as stokes Raman scattering or with a higher frequency that is known as anti-Stokes Raman scattering[72]. The shift in wavelength of the scattered light depends upon the chemical composition of the molecules responsible for scattering. The intensity of Raman scattering is proportional to the magnitude of the change in the molecular polarization. As described by Haynes, according to the Raman selection rule, the change in the molecular polarizability will be the result of the displacement of the constituent atoms from the equilibrium positions as the result of the molecular vibrations[73]. Raman spectrum can be treated as a fingerprinting tool for different compounds. Therefore, the Raman-obtained spectrum of the analyte can be used as qualitative analysis for unknown samples or a mixture of components.

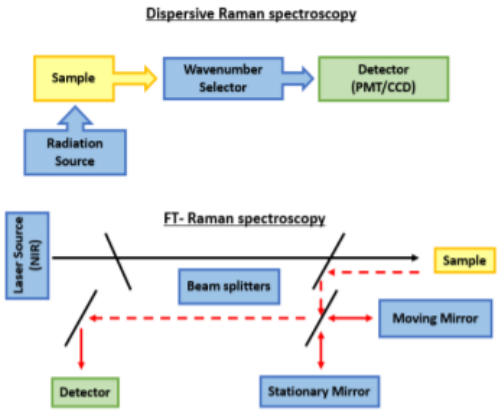


Figure 2.7: Raman Instrumentation (SEM)[6]

### 2.6.3 Fourier-transform infrared spectroscopy

Infrared spectroscopy is an excellent chemical analysis technique. Analysis of infrared spectra can tell you what molecules are present in a sample and at what concentrations; this is why infrared spectroscopy is useful. Several types of infrared spectrometers exist but the most commonly used are Fourier-transform infrared spectrometers. An schematic view of the method is shown in figure 2.8. A plot of measured infrared light intensity versus a property of light is called an infrared spectrum, by convention, the x-axis of an infrared spectrum is plotted with a high wavenumber to the left and a low wavenumber to the right. Plots of your FTIR spectra should always follow this convention. It can be expressed in absorbance units which measure the amount of light absorbed by the samples.

Using Beer's Law the concentration of the molecules can also be related to the concentration of the molecules where the height or area of a peak in an absorbance spectrum is proportional to concentration. The y-axis of an infrared spectrum can also be plotted in units called percent transmittance (%T), which measures the percentage of light transmitted by a sample.

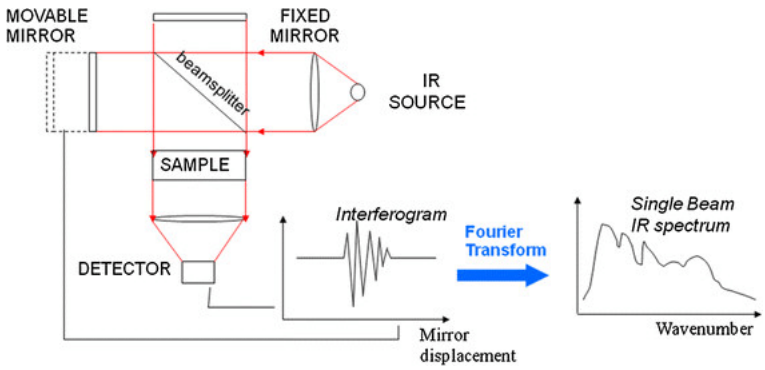


Figure 2.8: FTIR spectroscopy scheme[7]

### 2.6.4 Scanning Electron Microscope Energy-dispersive X-rays

The scanning electron microscope is the most widely used type of electron microscope, it examines microscopic structure by scanning the surface of materials with high resolution and depth of field that gives a three-dimensional appearance to its image. The image formation in SEM consists in a focused electron beam that scans over the surface area of a specimen[8]. It consists mainly of an electron gun that can be either thermionic or field emission type, a series of electromagnetic lenses and apertures as described in figure 2.9[8].

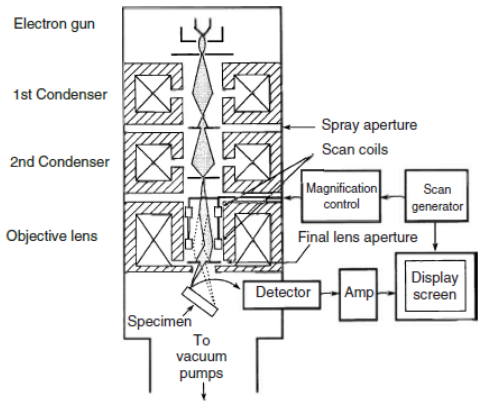


Figure 2.9: Structure of a scanning electron microscope (SEM)[8]

When high-energy electrons strike a specimen, they produce either elastic or inelastic scattering. Elastic scattering produces back-scattered electrons(BSEs), which are incident electrons scattered by atoms in the specimen. Inelastic scattering produces secondary electrons (SEs), which are electrons ejected from atoms in the specimen. BSEs are typically deflected from the specimen at large angles and with little energy loss; they typically retain 60–80% of the energy of incident electrons. In contrast, SEs are typically deflected at small angles and show much lower energy compared with incident electrons[74]. BSEs provide information about the composition of the sample as this signal is generated deeper in the sample. On the other hand, SEs comes from the surface of the sample which provides us with information about the topography of the sample, these electrons can add information about the composition of the material, but it is not the principal feature.

Energy dispersive spectroscopy (EDS) is a technique mostly employed for qualitative analysis of materials as well as a semi-quantitative outcome. SEM instrumentation is often equipped with an EDS detector and source allowing the chemical analysis of samples[75]. The detection limit in EDS depends on sample surface conditions, with a smooth surface, a lower detection limit is expected. EDS detects major and minor elements with a concentration of 10 wt% in the first case and between 1 - 10wt% in the second. In bulk materials, the detection limit is 0.1 wt% due to this EDS cannot detect trace elements ([] < 0.01 wt%)[76].

### 2.6.5 X-Ray Powder Diffraction (XRD)

Diffraction occurs when light is scattered by a periodic array with long-range order, producing constructive interference at specific angles. The atoms in a crystal are periodically arranged, thus diffracting light. The wavelength of an X-ray is similar to the distance between atoms, Powder X-ray Diffraction (PXRD) techniques use this principle to elucidate the crystalline nature of materials. The scattering of X-rays from atoms produces a diffraction pattern containing information about the crystal's atomic arrangement. Amorphous materials like glass do not have a periodic array with long-range order; they do not produce any significant peaks in the diffraction pattern.

Powder XRD is a compact advanced instrument, in figure 2.10, a schematic form of the technique is displayed. It has various salient features and new accessories like variable temperature assembly and humidity chamber that can further expand the horizon of its applications by providing information on the effect of temperature and humidity on the nature of the material. When an X-ray falls over a crystal, it diffracts in a pattern characteristic of its structure. In powder X-ray diffraction, the diffraction pattern is obtained from a powder of the material, rather than an individual crystal. Powder diffraction is often easier and more convenient than single-crystal diffraction as it does not require individual crystals. A diffraction pattern plots intensity against the angle of the detector, $2\theta$. The result obtained is called a diffractogram. In a diffraction pattern, the peak position depends upon the wavelength. Absolute intensity (number of X-rays observed in a given peak) may vary by instrumental and experimental parameters. Diffractometers can be operated both in transmission and reflection configurations. The reflection one is more common. Interactions between the incident X-ray beam and the sample produce intense reflected X-rays by constructive interference when conditions satisfy Bragg's Law. This law describes the general relationship between the wavelength of the incident X-rays, the incident angle of the beam, and the spacing between the crystal lattice planes of atoms. Constructive interference occurs when the differences in the travel path of the incident X-rays are equal to an integer multiple of

the wavelength[77].

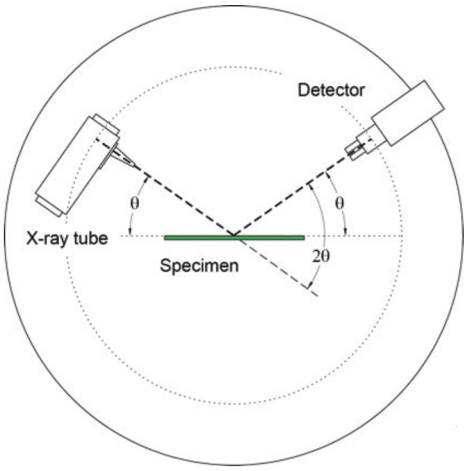


Figure 2.10: X-ray Powder Diffraction scheme)[9]

### 2.6.6 UV-Visible Spectroscopy

Ultraviolet-Visible Spectroscopy is a spectrophotometric technique that measures the intensity of light in Ultraviolet (10-400 nm) and Visible (400-800) regions of the spectrum as a wavelength function that are expressed usually in nanometers (nm). Figure 2.11 shows an illustration on the working principle of the method. A specific wavelength of the source is absorbed by the analyte in the sample and the signal is directly proportional to the concentration. This is because as the amount of the analyte increases, the absorption of light increases linearly while the transmission decreases in an exponential manner. In the UV-Vis region, radiation absorption is dependent on the electronic configuration of the absorbing species like complexes, ions, molecules, or complexes[78].

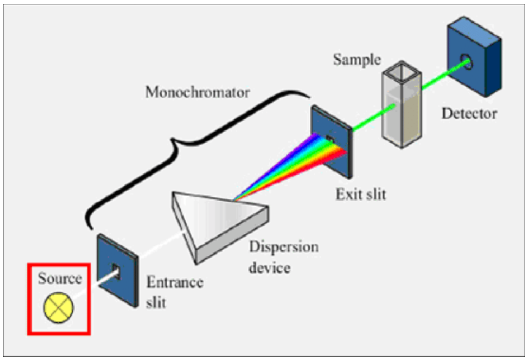


Figure 2.11: UV-Vis spectroscopy scheme[10]

Electronic energy levels consist of various vibrational energy levels and each vibrational energy level is composed of other rotational energy levels. When a molecule interacts with a photon a transition in this electronic state can be induced if the difference in energy of this level matches the photon energy. The radiation absorbed by the analyte is measured and plotted in order to develop the spectrum. Therefore, typically UV-Vis spectrum is a plot of wavelength or frequency versus the absorption intensity[78]. Diffuse reflectance is a particular technique that take place when light impacts the surface of a material and the signals are partially reflected and transmitted. It can be described as the reflection of light in all directions with small interfaces on an irregular surface where small surfaces oriented at all possible angles forms interfaces that can be considered. Detected light can possess a combination signal of the emitted and reflected components[79]. When photons hit the samples, the energy absorbed by the molecule causes an electron excitation from the highest occupied molecular orbital (HOMO) to the lowest unoccupied molecular orbital (LUMO). The band gap refers to the difference in energy between the two states.

### 2.6.7 Fluorescence Microscopy

The application of fluorescence to microscopy has helped the development in biological field as information about the structures of the cells and the exact location of the molecules. It also allows to quantitate the amounts of certain molecules within the cell, to measure ionic concentrations difference as the molecular dynamics[80]. Fluorescence is a result of absorbance in specific range of wavelengths resulting in longer wavelength photon emission in after the relaxation of excited electrons by organic and inorganic species. Fluorescence microscope works on the principle of filtering, trapping and detecting the signal at a higher unique wavelength. Source light is sent to an exciter filter, selecting the excitation wavelength then directed to a dichroic mirror which reflects light only in the selected excitation wavelength; this beam passes through the sample and emitted rays are collected and magnified by an objective lens and sent to a barrier filter. Selected wavelengths are sent to eyepiece detector for optical viewing or digitalization of the image[81]. Figure 2.12 shows a schematic illustration of the fluorescence microscopy.

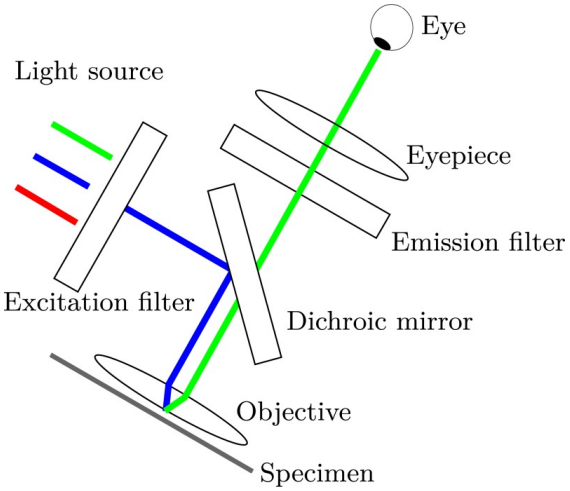


Figure 2.12: Fluorescence microscopy illustration)[11]

# Chapter 3

# Methodology

This section provides a description of the reagents, preparation of solutions, substitution procedures and experimental conditions. In addition, the equipment used to develop this work is detailed.

## 3.1 Experimental Part

### 3.1.1 Reagents and Solutions

Distilled water was the only solvent used in this process. Calcium Chloride ($CaCl_2$, ACS reagent, +99%) and ammonium phosphate dibasic ($(NH_4)_2HPO_4$, reagent grade, +98.0%), obtained from Sigma Aldrich Co., were used as the Ca and phosphate components respectively. Cerium was obtained as Cerium Sulfate ($Ce(SO_4)_2$, cerium Sulfate (III) ($CeSO_4$) (reagent grade, +99%)) obtaind from the same corporation.

### 3.1.2 Hydroxyapatite synthesis

Hydroxyapatite was synthesized by the hydrothermal method. 1.11 g of Calcium Chloride was dissolved in 25 ml of distilled water and then added drop by drop to a solution containing 0.69 g of Ammonium Phosphate dibasic while stirring. The final solution was located in a reactor and then introduced to the oven for 24 hours at 125 ºC. pH level was reduced through distilled water baths. The sample was dried at 60ºC for 24 hours.

### 3.1.3 Hydroxyapatite doping with Cerium

Samples with Cerium substitution were synthesized with the same hydrothermal method using 5%, 10%, 15%, 20%, and 25% concentration of the foreign ion, in table 3.1 is described the composition of each sample. Cerium sulfate was dissolved in all occasions with 25 ml of Distilled water while stirring at 60ºC for 30 minutes and then added drop by drop to 0.69 g of Ammonium Phosphate dibasic. The samples were placed in a reactor each and then inside

| **Sample Preparation** | | | | | | | |
|---|---|---|---|---|---|---|---|
| Samples | [Ce] (mmol) | Cerium Sulfate (g) | Calcium Chloride (g) | Ammonium Phosphate (g) | Stove time (h) | $pH_o$ level | $pH_f$ level |
| Raw HAp | 0 | 0 | 1.11 | 0.69 | 24 | 11 | 8 |
| $Ce_{0.5}$-HAp | 0.5 | 0.1661 | 1.0543 | 0.69 | 24 | 11 | 8 |
| $Ce_1$-HAp | 1 | 0.3322 | 0.9988 | 0.69 | 24 | 11 | 8 |
| $Ce_{1.5}$-HAp | 1.5 | 0.4984 | 0.9433 | 0.69 | 72 | 11 | 8 |
| $Ce_2$-HAp | 2 | 0.6645 | 0.8878 | 0.69 | 72 | 11 | 8 |
| $Ce_{2.5}$-HAp | 2.5 | 0.8306 | 0.7102 | 0.69 | 24 | 11 | 8 |

Table 3.1: Sample preparation of HAp doped with different concentrations of Cerium

an oven for 24 hours at 125ºC. pH level was reduced using distilled water baths. All samples were dried at 60ºC for 24 hours.

## 3.2 Structural and Morphological Characterization

Samples were characterized using Fourier Transform Infrared Spectroscopy, Raman Spectroscopy, Scanning Electron Microscopy, and Energy Dispersive X-Ray Analysis.

### 3.2.1 Fourier Transform Infrared Spectroscopy

Ceria, raw hydroxyapatite and substituted hydroxyapatite were characterized using Fourier Infrared Spectroscopy. Samples were analyzed using a spectrometer Agilent Cary 630 FT-IR (Diamond ATR) in the range of 4000–600 $cm^{-1}$, with a spectra resolution < 2 $cm^{-1}$ as seen in figure 3.1. Samples were acquired in the form of Transmittance vs wavenumber at room temperature.

Figure 3.1: Agilent Cary 630 FT-IR (Diamond ATR) spectrometer

### 3.2.2 Raman Spectroscopy

Figure 3.2 shows LabRAM HR Evolution Raman microscope, which was employed to perform Raman Spectroscopy of the samples in the range of UV to NIR wavelengths (200 nm - 2200 nm). Characterization was made using an excitation wavelength of 633nm.

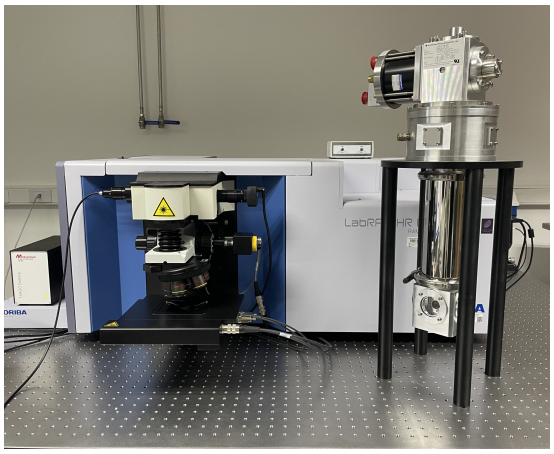

Figure 3.2: LabRAM HR Evolution Raman microscope

### 3.2.3 Scanning Electron Microscopy and EDS

analysis was carried out in a Phenom Pro X scanning electron microscope coupled with an EDX spectroscopy detector. The acceleration voltage used was 10 kV with a maximum resolution of 10 nm. EDX analysis provide us with compositional information of the samples.

Figure 3.3: Phenom Pro X scanning electron microscope used SEM analysis.

### 3.2.4 Ultraviolet-Visible Spectroscopy

Reflectance and energy band gap calculations were obtained by using LAMBDA 1050+ UV/Vis/NIR Spectrophotometer to obtain the different information. The praying Mantis set up was selected for the experiment due to the powder form of the samples.

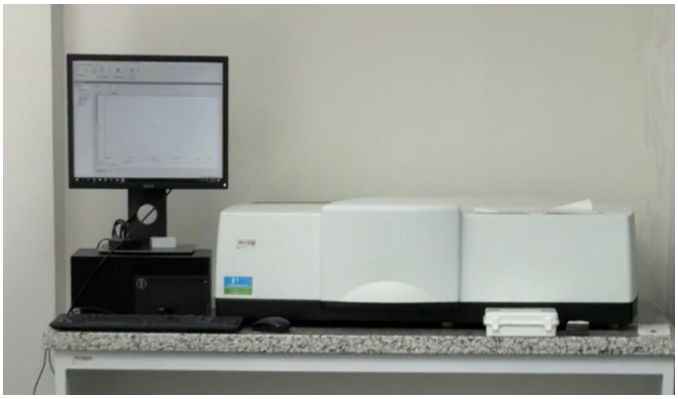

Figure 3.4: LAMBDA 1050+ UV/Vis/NIR Spectrophotometer used for UV-Vis measurements

### 3.2.5 Fluorescence Spectroscopy

Olympus BX63 Automated Fluorescence microscope was employed to analyzee the optical response in the samples using different filters and magnifications. The equipment used for this section corresponds to figure 3.3.

Figure 3.5: Olympus BX63 Automated Fluorescence microscope

# Chapter 4

# Results & Discussion

## 4.1 Structural and Morphological Characterization

### 4.1.1 Fourier Transform Infrared Spectroscopy

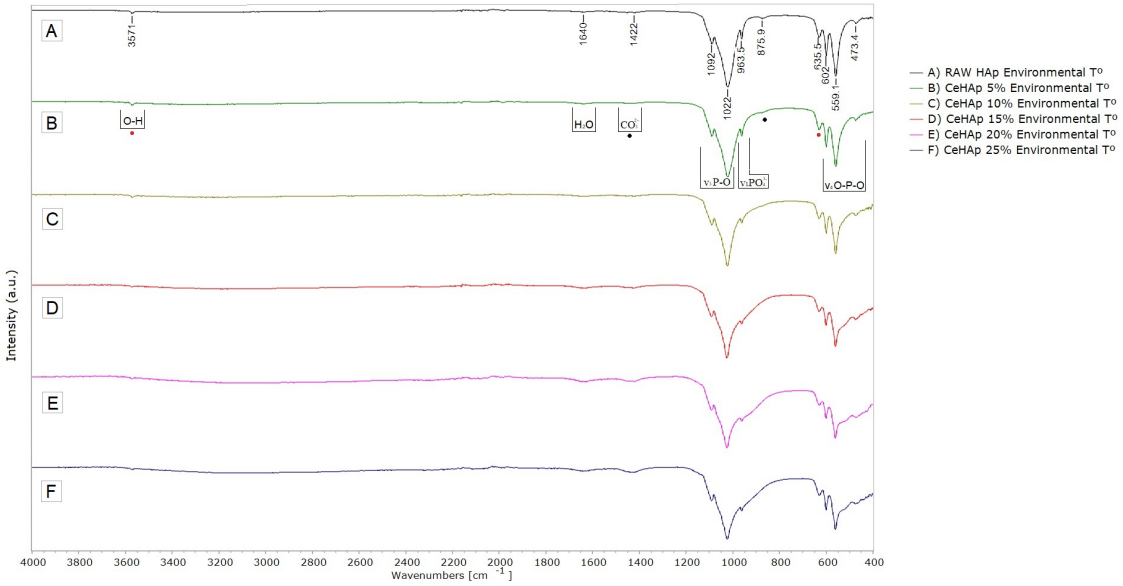


Figure 4.1: FTIR spectra of RAW HAp and Doped HAp samples at room temperature. A) RAW HAp, B) CeHAp 5%, C) CeHAp 10%, D) CeHAp 15%, E) CeHAp 20%, and F) CeHAp 25%

By FTIR spectroscopy, the reported modes of vibration from the characteristic functional groups present in HAp powder samples were analyzed. Figure 4.1 shows the spectra corresponding to non-calcined samples which shows the previously reported bands. Bands present at around 473 $cm^{-1}$, 559 $cm^{-1}$,and 602 $cm^{-1}$ are due to the bending in $\nu_4$ P-O-P group[82 68]. Peaks exhibit in the zone of 963 $cm^{-1}$ are consequence of the $\nu_1$ $PO^{3-}{}_4$ group stretching meanwhile in the region around 1022 $cm^{-1}$ and 1092 $cm^{-1}$ is attributed to the $\nu_3$ asymmetrical stretching[83 67]. Singh, et al. reported that around 1640 $cm^{-1}$ it can be notice the presence of water molecules consequence absorbed by the samples. The stretching of the O-H group is displayed at 3671 $cm_{-1}$ and 635 $cm^{-1}$ bands. In addition, $CO^{2-}{}_3$ presence is confirmed with the bands in the area of 1420 $cm^{-1}$ and 875 $cm^{-1}$[84 85] (See table 4.1 for complete data). In the case of the environmental temperature samples, $CO^{2-}{}_3$ at 875 $cm^{-1}$ was absorbed by the rise of the stretching of the $\nu_1$ phosphate group as well as growth as well in one of the peaks related with the $\nu_4$ bending when the concentration of cerium increases. No significant changes in the regions of the bands presented was noted besides the peaks broadening which suggest a change in the vibrational modes of the structure due to the foreign ion introduction. The presence of the carbonates indicates that $PO^{3-}{}_4$ groups were replaced by $CO^{2-}{}_3$ in a reaction between the CeHap samples and carbon dioxide present in the air[86]. Peak formation varies inversely as the concentration of cerium increases, O-H, P-O and O-P-O bonds shows weakening of the bands as the peaks decreases suggesting interactions given by the substitution process. When $Ce^{4+}/Ce^{3+}$ replaces $Ca^{2+}$ ions, $OH^-$ group must undergo a transformation as suggested by Serret, et al[87]. into $O^{2-}$ due to the breakage of the electric charge balance within the HAp. Phosphate groups variations may come as well due to the ions exchange and posterior variation in the bonding forces between ions[60 41].

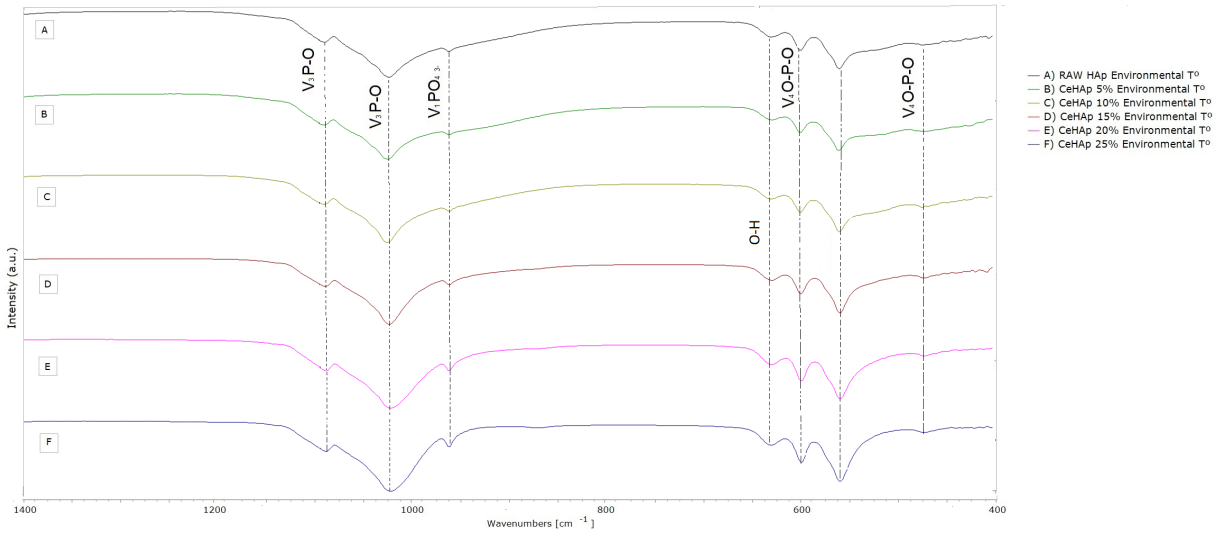


Figure 4.2: FTIR spectra of RAW HAp and Doped HAp samples treated at 200 ºC. A) RAW HAp, B) CeHAp 5%, C) CeHAp 10%, D) CeHAp 15%, E) CeHAp 20%, and F) CeHAp 25%

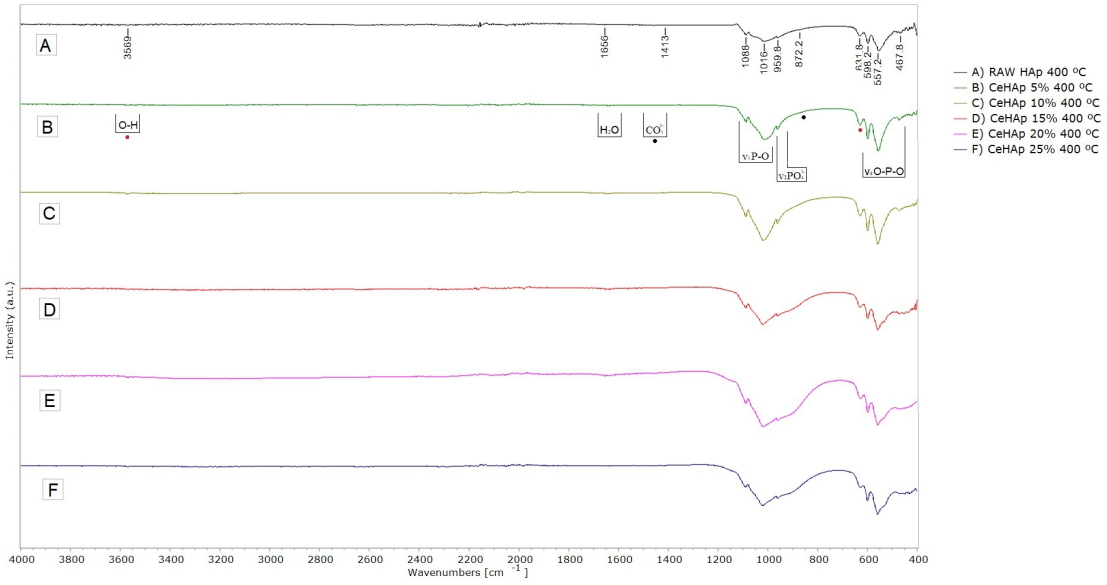


Figure 4.3: FTIR spectra of RAW HAp and Doped HAp samples treated at 400 ºC. A) RAW HAp, B) CeHAp 5%, C) CeHAp 10%, D) CeHAp 15%, E) CeHAp 20%, and F) CeHAp 25%

Figure 4.2 shows the FTIR bands zoomed in the region of 1400 $cm^{-1}$ to 400 $cm^{-1}$ where the peaks corresponding to the characteristic vibrational modes of HAp are displayed. As the temperature was increased to 200 ºC, there was not a variation in the behaviour of the samples, leading to a similar graph as the first shown. At 400ºC the bands changes remain in the same direction but with a generalized intensity decrease in the peaks which suggest changes in molecular structure. Samples calcined at 600 ºC also varies in the same way, nevertheless, it can be notice that the sample containing the most cerium percentage (25%) peaks start to broaden, letting new band arises around 500 $cm^{-1}$ and eliminating the $OH^-$ signal at around 3570 $cm^{-1}$ as shown in figure 4.3. This is also shown in figure 4.4 for samples subjected to 800 ºC heat treatment, where the elimination of the signal corresponding to OH group can be due to the loss of water molecules. In table 4.1, it is displayed all peak information about the samples.

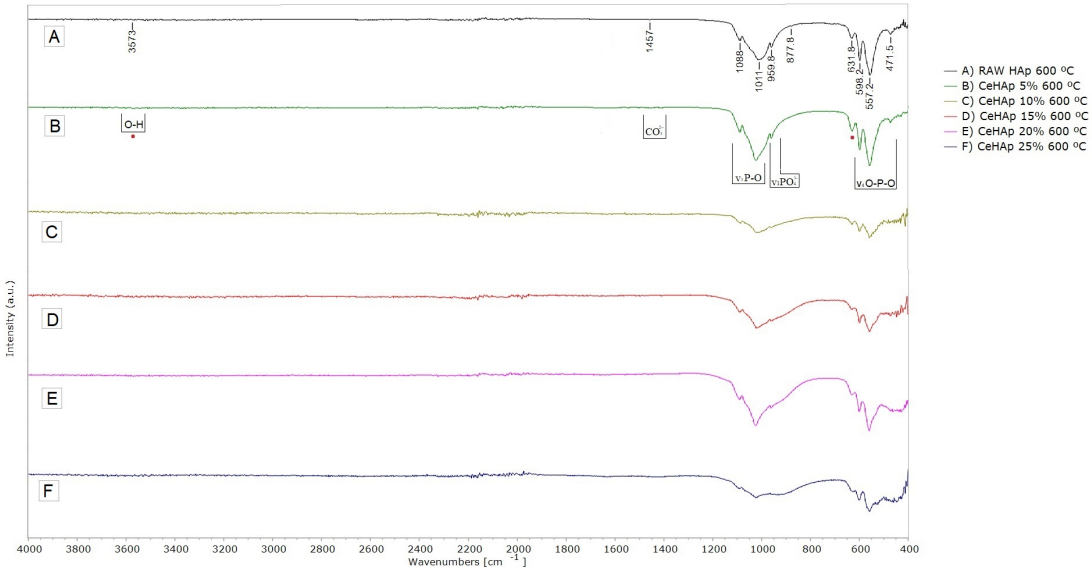


Figure 4.4: FTIR spectra of RAW HAp and Doped HAp samples calcined at 600 ºC. A) RAW HAp, B) CeHAp 5%, C) CeHAp 10%, D) CeHAp 15%, E) CeHAp 20%, and F) CeHAp 25%

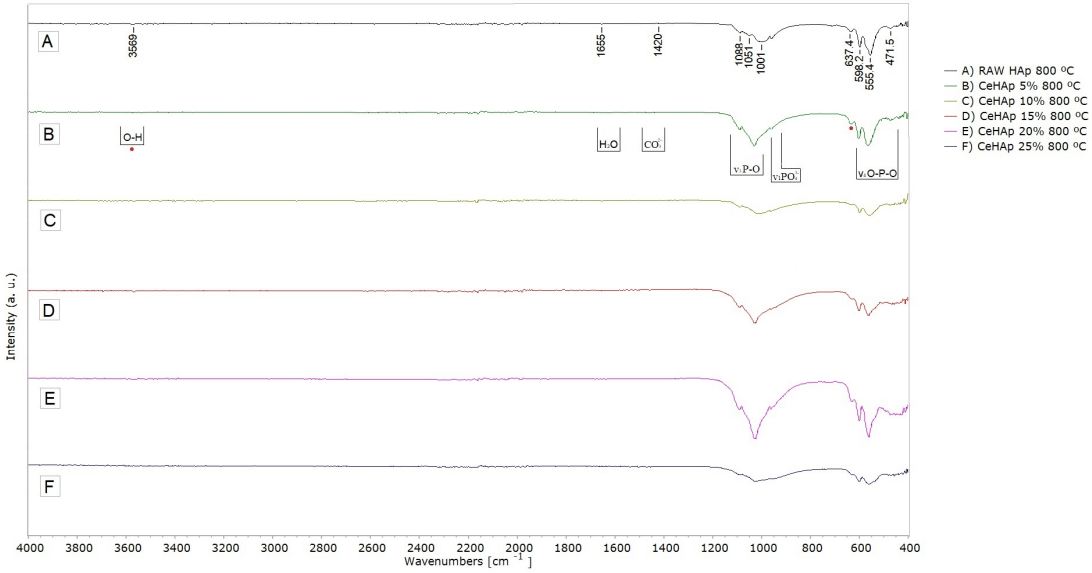


Figure 4.5: FTIR spectra of RAW HAp and Doped HAp samples calcined at 800 ºC. A) RAW HAp, B) CeHAp 5%, C) CeHAp 10%, D) CeHAp 15%, E) CeHAp 20%, and F) CeHAp 25%

| **FTIR peak values for elemental ions** | | | | | | | | | |
|---|---|---|---|---|---|---|---|---|---|
| Samples | T (ºC) | O - H | $CO^{2-}_3$ | P - O *Type*$\nu_3$ | $PO^{3-}_4$ *Type*$\nu_3$ | $PO^{3-}_4$ *Type*$\nu_3$ | O-H | O-P-O $\nu_4$ | O-P-O $\nu_4$ |
| Raw HAp | 25 | 3571 | 1422 | 1092 | 1022 | 964 | 635 | 602 | 561 |
| $Ce_{0.5}$-HAp | 25 | 3570 | 1421 | 1090 | 1022 | 962 | 634 | 600 | 561 |
| $Ce_1$-HAp | 25 | 3569 | 1422 | 1090 | 1024 | 964 | 632 | 600 | 559 |
| $Ce_{1.5}$-HAp | 25 | 3572 | 1422 | 1092 | 1026 | 962 | 634 | 605 | 560 |
| $Ce_2$-HAp | 25 | 3571 | 1422 | 1094 | 1026 | 964 | 632 | 602 | 561 |
| $Ce_{2.5}$-HAp | 25 | 3570 | 1421 | 1092 | 1024 | 964 | 635 | 600 | 561 |
| Raw HAp | 200 | 3571 | 1421 | 1090 | 1024 | 962 | 632 | 600 | 560 |
| $Ce_{0.5}$-HAp | 200 | 3571 | 1418 | 1088 | 1025 | 962 | 633 | 600 | 561 |
| $Ce_1$-HAp | 200 | 3571 | 1422 | 1090 | 1023 | 963 | 632 | 600 | 559 |
| $Ce_{1.5}$-HAp | 200 | 3571 | 1426 | 1090 | 1025 | 962 | 632 | 600 | 560 |
| $Ce_2$-HAp | 200 | 3571 | 1422 | 1090 | 1020 | 962 | 632 | 600 | 560 |
| $Ce_{2.5}$-HAp | 200 | 3569 | 1420 | 1090 | 1023 | 962 | 635 | 600 | 560 |
| Raw HAp | 400 | 3569 | 1420 | 1088 | 1013 | 960 | 632 | 598 | 556 |
| $Ce_{0.5}$-HAp | 400 | 3573 | 1422 | 1088 | 1013 | 960 | 630 | 598 | 557 |
| $Ce_1$-HAp | 400 | 3573 | 1415 | 1088 | 1019 | 962 | 630 | 598 | 557 |
| $Ce_{1.5}$-HAp | 400 | 3569 | 1420 | 1088 | 1020 | 960 | 630 | 598 | 561 |
| $Ce_2$-HAp | 400 | 3570 | 1420 | 1088 | 1019 | 960 | 630 | 598 | 561 |
| $Ce_{2.5}$-HAp | 400 | 3571 | 1420 | 109 | 1021 | 962 | 629 | 600 | 561 |
| Raw HAp | 600 | 3573 | 1413 | 1088 | 1011 | 960 | 632 | 598 | 557 |
| $Ce_{0.5}$-HAp | 600 | 3573 | 1413 | 1088 | 1024 | 962 | 630 | 598 | 558 |
| $Ce_1$-HAp | 600 | 3575 | 1416 | 1088 | 1015 | 960 | 632 | 598 | 561 |
| $Ce_{1.5}$-HAp | 600 | 3570 | 1409 | 1090 | 1020 | 962 | 634 | 600 | 561 |
| $Ce_2$-HAp | 600 | 3571 | - | 1090 | 1024 | 962 | 630 | 600 | 560 |
| $Ce_{2.5}$-HAp | 600 | - | 1414 | 1092 | 1025 | 960 | 626 | 600 | 557 |
| Raw HAp | 800 | 3569 | 1420 | 1088 | 1051 | 1001 | 637 | 598 | 556 |
| $Ce_{0.5}$-HAp | 800 | 3571 | 1422 | 1090 | 1031 | 962 | 632 | 600 | 563 |
| $Ce_1$-HAp | 800 | 3568 | 1420 | 1090 | 1010 | 962 | 636 | 598 | 561 |
| $Ce_{1.5}$-HAp | 800 | 3568 | 1420 | 1090 | 1028 | 962 | 632 | 602 | 563 |
| $Ce_2$-HAp | 800 | 3565 | 1428 | 1090 | 1027 | 962 | 632 | 600 | 561 |
| $Ce_{2.5}$-HAp | 800 | - | - | 1090 | 1024 | 962 | 628 | 600 | 563 |

Table 4.1: Sample preparation of HAp doped with different concentrations of Cerium

### 4.1.2 X-Ray Diffraction

X-ray powder diffraction profiles of the samples were studied to analyze the crystallographic characteristics of each one. According to previous studies, JCPDS card no. 09-432 key diffraction peaks of hydroxyapatite are (0 0 2), (2 1 1), (1 1 2), (3 0 0), (2 0 2), (3 0 1), (3 1 0), (2 2 2), (2 1 3) and (0 0 4) crystal lattice planes[88 67]. All planes are present in the pure samples of HAp, as in most cases. RAW HAp and Ce doped HAp peak position present no changes as the concentration of cerium was increased in environmental conditions. Raw HAp exhibits well defined peaks however when Ce ions are added, peaks starts to broaden which implies a reduction in the crystallinity degree due to the incorporation of the dopant into the HAp lattice. For the structural defects with low cristallinity and high resorbability by body fluids, this nanomaterials are preferred as a choice as drug carriers[67]. The different charge compensation mechanism due to non-isomorphous substitution among Ce and Ca ions may be one of the causes in this effect additionally suggesting a nanometric size particles[41]. Ionic radius of $Ca^{2+}$ is of 1 Åis greater than $Ce^{4+}$ (0.97 Å) but minor to $Ce^{3+}$ (1.19 Å) radius, therefore a variation in the lattice parameters is expected due to the reduction of the ion. Intesrstitial defects are produced due to this reduction. In figure 4.6, all the samples exhibits the characteristics described above which propose a successful doping of the Ce ions into the hydroxyapatite structure by hydrothermal synthesis with different concentrations avoiding any significant change at environmental temperature.

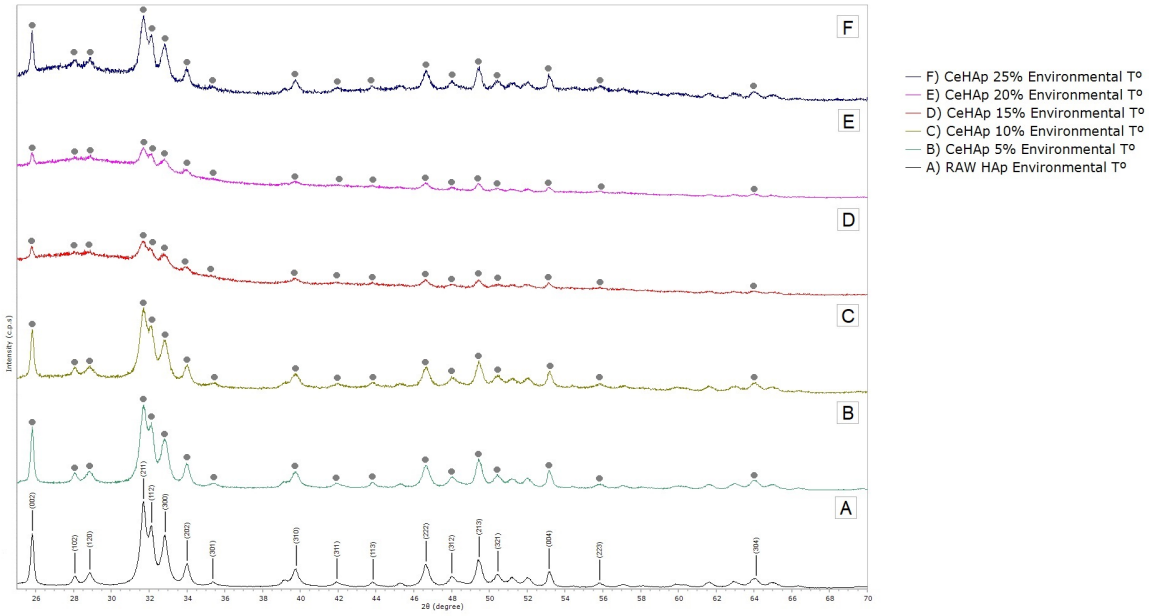


Figure 4.6: XRD patterns of samples at Environmental ºT. A) RAW HAp, B) 5% CeHAp, C) 10% CeHAp, D) 15% CeHAp, E) 20% CeHAp and F) 25% CeHAp

At 200 ºC the XRD pattern remains in the same state as previously mentioned. When samples where submitted

to 400 ºC the planes (1 0 2) and (1 2 0) and (2 2 2), suffered alterations when the Ce content was 20%, described in figure 4.7, suggesting a struggle in the HAp lattice to host completely ions[66]. When the concentration reaches 25% level, the peaks return to a very similar state as before. Less content of $Ce^{3+}$ is expected in this last sample. Figure 4.8 displays the patterns of samples at 600 ºC, the behaviour mentioned starts to been notice at earlier in the concentration scale with the 15% and 20% samples that besides having an alteration in the peaks mentioned before it also has distortions in the (3 1 2) plane, that suggest a change in the crystal structure of the material. For the 800 ºC batch presented in figure 4.9, it started with small alterations in the 10% sample but increases likewise concentration, at 20% a change in the apatite phase is proposed as peaks are formed in a different arrangement.

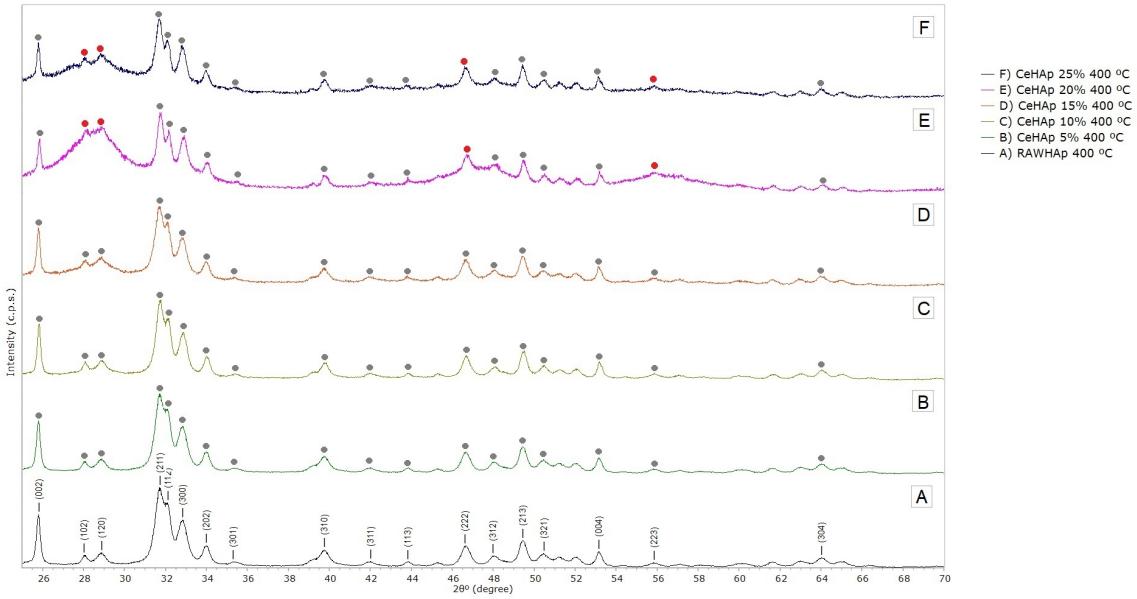


Figure 4.7: XRD patterns of samples at 400 ºC. a) Raw HAp, b) 5% CeHAp, c) 10% CeHAp, d) 15% CeHAp, e) 20% CeHAp and f) 25% CeHAp.

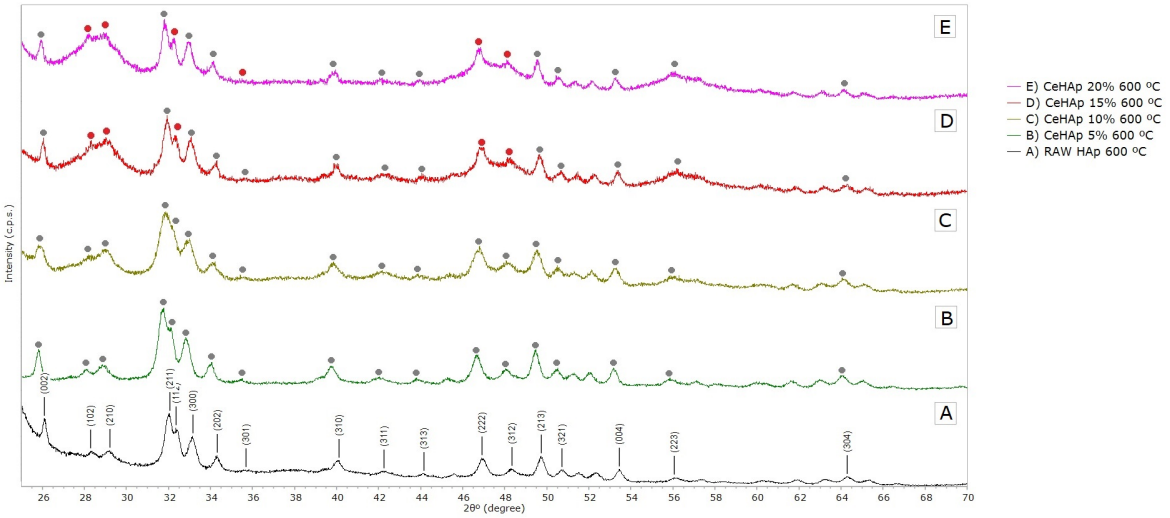


Figure 4.8: XRD patterns of samples calcined at 600 ºC. a) Raw HAp, b) 5% CeHAp, c) 10% CeHAp, d) 15% CeHAp, e) 20% CeHAp and f) 25% CeHAp

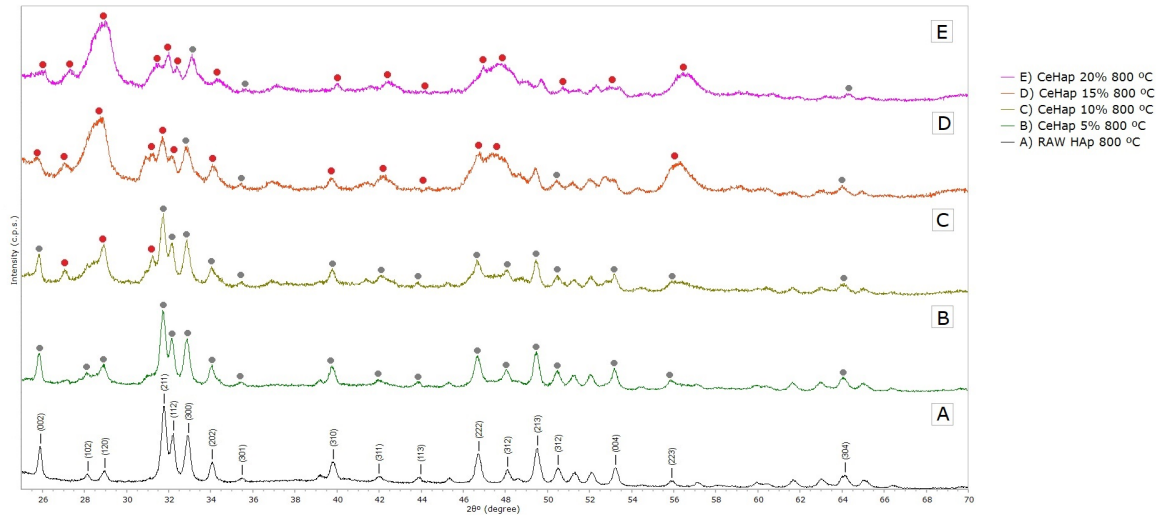


Figure 4.9: XRD patterns of samples at 800 ºC. a) Raw HAp, b) 5% CeHAp, c) 10% CeHAp, d) 15% CeHAp, e) 20% CeHAp and f) 25% CeHAp

### 4.1.3 Raman Spectroscopy

Vibrational modes of characteristic molecules in hydroxyapatite as in Ce-hydroxyapatite in the frequency of 300 to 1200 $cm^{-1}$ as formerly reported in the literature. Raman spectra of Pure Hydroxyapatite (figure 4.10) manifest a strong characteristic peak in the zone around 963 $cm^{-1}$ awarded to $\nu_1$ of the $PO_4^{3+}$ group corresponding to the symmetrical stretching of the P - O bond. In addition peaks two peaks corresponding to asymmetrical stretching $\nu_3$ P - O mode included with single signal peaks of bending modes $\nu_2$ and $\nu_4$ [66]. Bands are assigned to the internal vibrational modes of $PO_4^{3+}$ groups. From the spectral analysis it can be inferred that at a growing Ce concentration, the dominant peak switches to the zone around 463 $cm^{-1}$ suggesting an interaction between the Ce ions and the $PO_4^{3+}$ group. This shift and broadening of the dominant peaks can be related to the effect of Ce substitution on the crystal structure of HAp, which can lead to lattice distortion, defects and disorder, which can affect the Raman-active modes of the HAp lattice. Peaks in the mentioned zone are broaden, indicating amorphous nature as the Ce ions are added. As the temperature is elevated to 200 ºC and 400 ºC, the tendency remains the same but the better sharped peaks start to been notice. At 600 ºC as well as in 800 ºC, which is shown in figure 4.11, well defined peaks emerge in the samples.

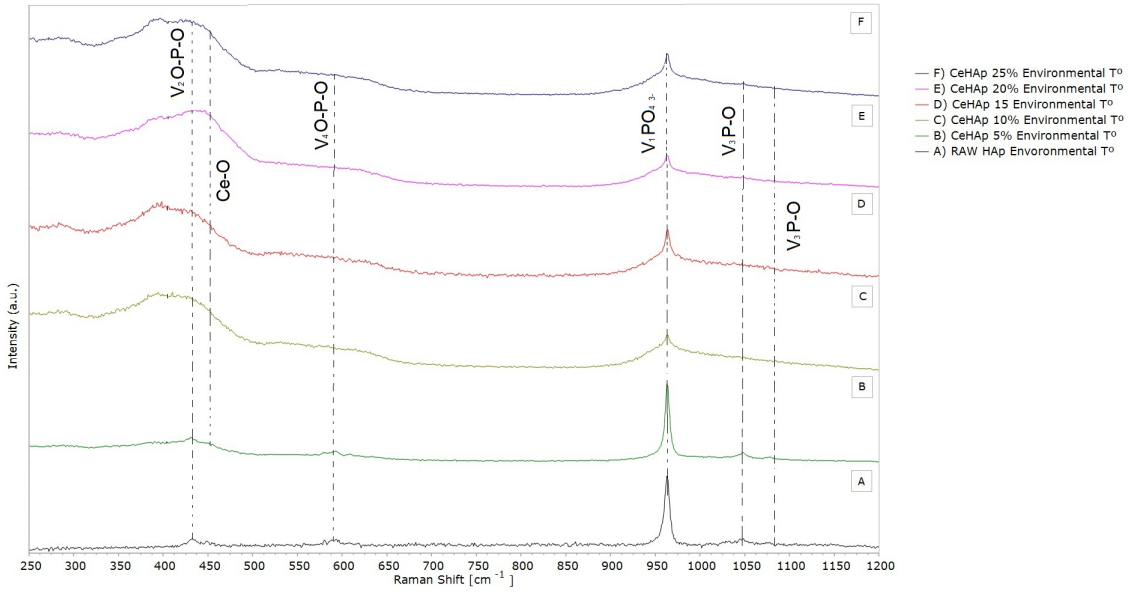


Figure 4.10: Raman spectra of samples at environmental temperature. a) Raw HAp, b) 5% CeHAp, c) 10% CeHAp, d) 15% CeHAp, e) 20% CeHAp and f) 25% CeHAp

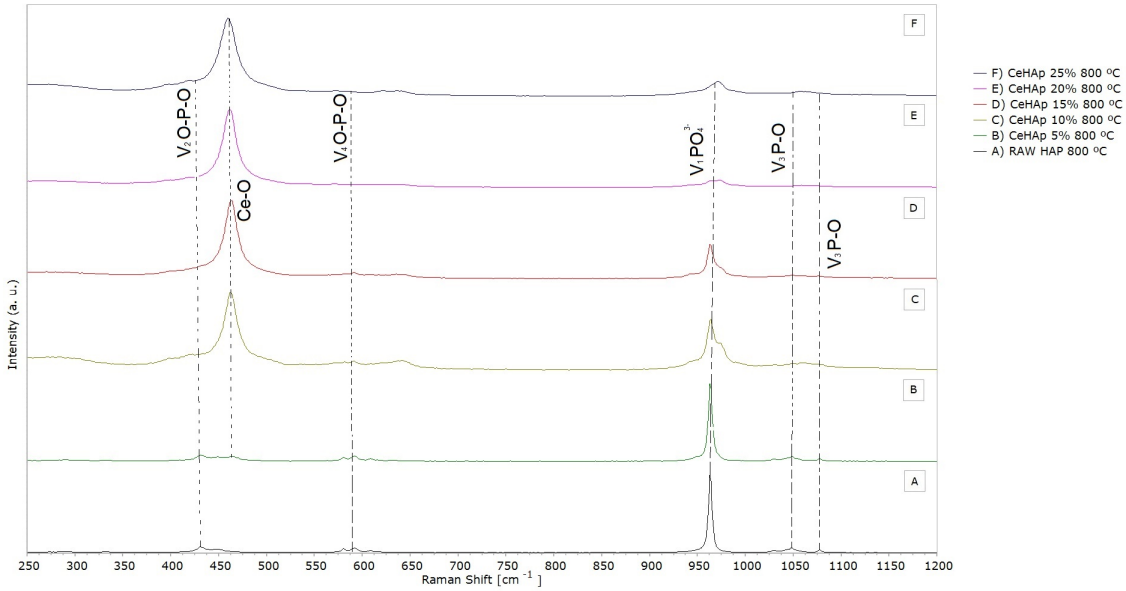


Figure 4.11: Raman spectra of samples at 800ºC. A) RAW HAp, B) 5% CeHAp, C) 10% CeHAp, D) 15% CeHAp, E) 20% CeHAp and F) 25% CeHAp

### 4.1.4 Scanning Electron Microscopy and EDS

SEM imaging by full BSEs with the same magnification for all samples is shown in Fig. 4.12. Micrographs show in 4.12A) hydroxyapatite doped in 10% cerium content at 800 ºC, 4.12B) 20% CeHAp at the same temperature while 4.12C) and 4.12D) the same content as mentioned above but at 800 ºC. Bright spots in the images are of cerium as the atomic number of the dopant is higher than any other HAp essential ion. A well-dispersed dopant is appreciable in the host-apatite. SEM images show many crystal clusters with irregular morphology in all samples and indicates a diminishing in particle agglomerations with the growing percentage of cerium with a decreasing particle size in the samples. The size of the particles in the HAp matrix can be influenced by the Ce ions concentration, as the concentration increases, it can lead to the formation of smaller particles due to its effect on the nucleation and growth rates during the synthesis process, where, an increase of the concentration may result in faster nucleation and growth rates while at lower concentrations, this processes becomes also slower leading to larger particle sizes. Temperature also takes place in the formation of smaller particles as it increases energy available for bond formation, which can lead to smaller crystals as seen in figure 4.13. In addition, temperature can lead to faster crystal growth leading to differences in crystal shape, producing sharper particles as in accordance to the change sharpness of the Raman peaks mentioned in the last section.

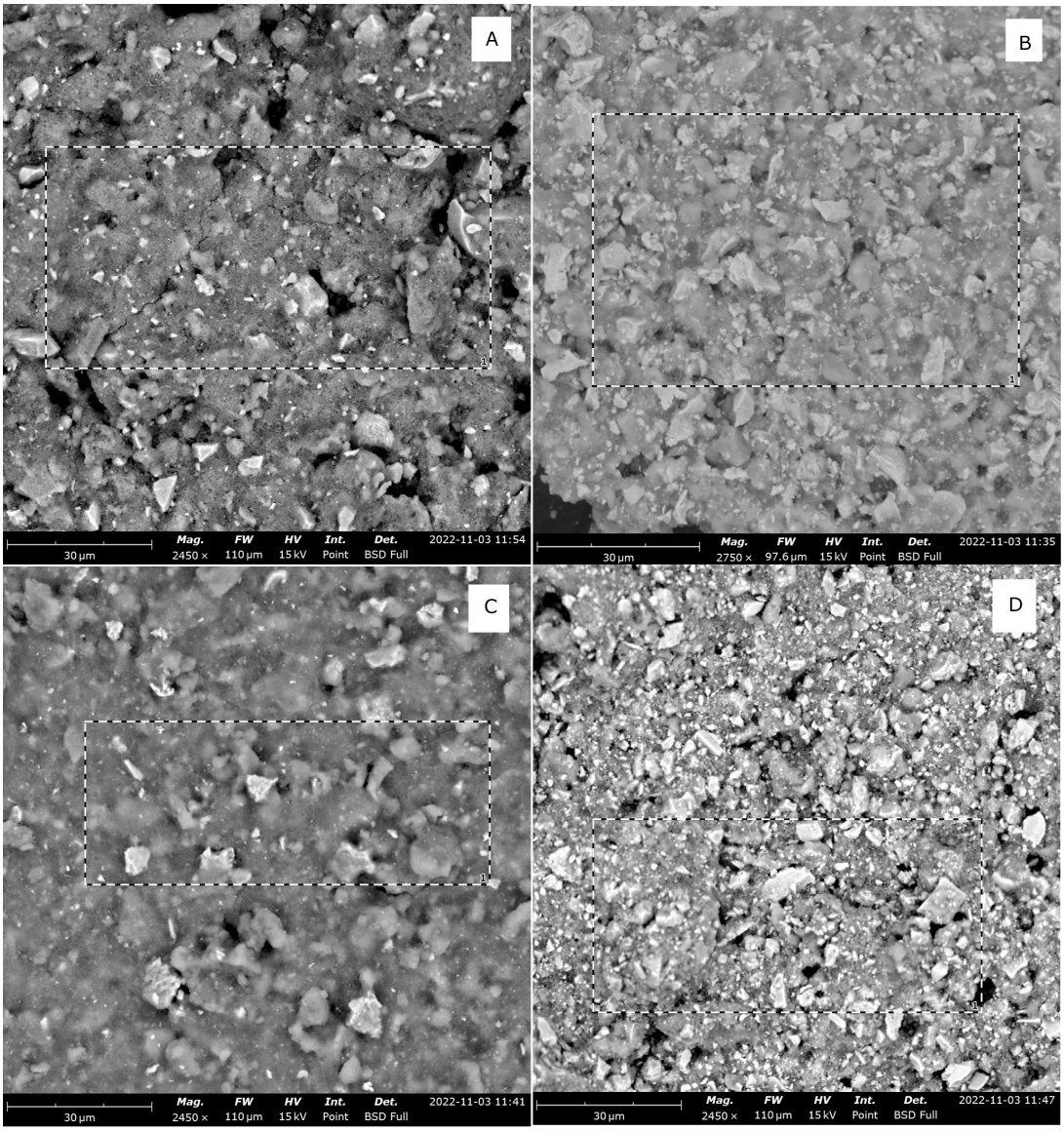


Figure 4.12: SEM imaging of samples. A) 10% CeHAp at 400ºC, B) 20% CeHAp at 400 ºC, C) 10% CeHAp at 800ºC, D) 20% CeHAp at 800 ºC

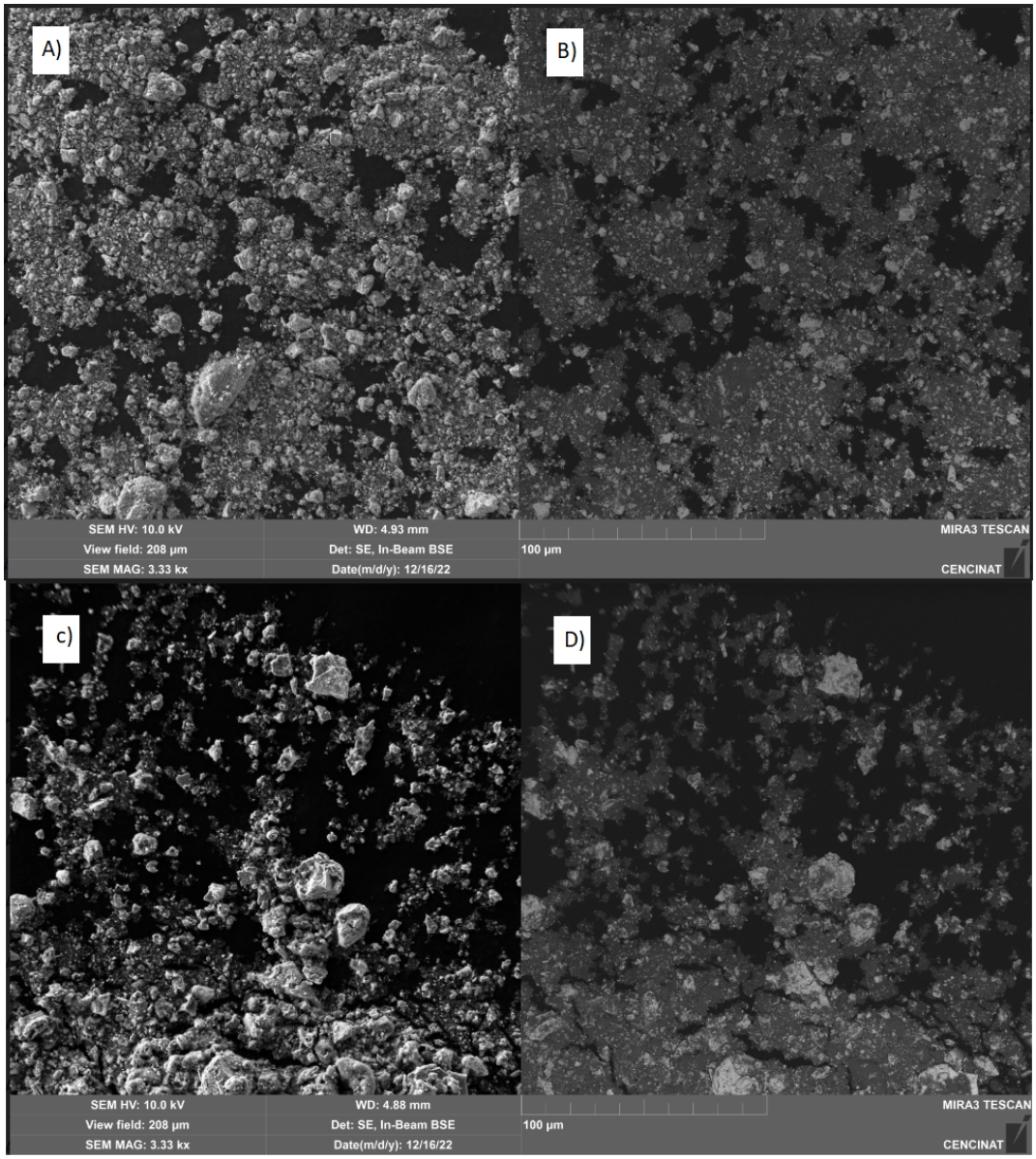


Figure 4.13: SEM imaging of samples. A) 20% CeHAp at 400ºC SE, B) 20% CeHAp at 400 ºC BSE, C) 20% CeHAp at 800ºC SE, D) 20% CeHAp at 800 ºC BSE

### EDS Analysis

Elemental composition peaks for Ce substituted HAp are shown in figure 4.14, the EDS spectra of 10% and 20% samples at 600 ºC and 800 ºC. Elemental hydroxyapatite ions (Ca, P, O) as well as Ce peaks related confirmed the apatite doped formation.

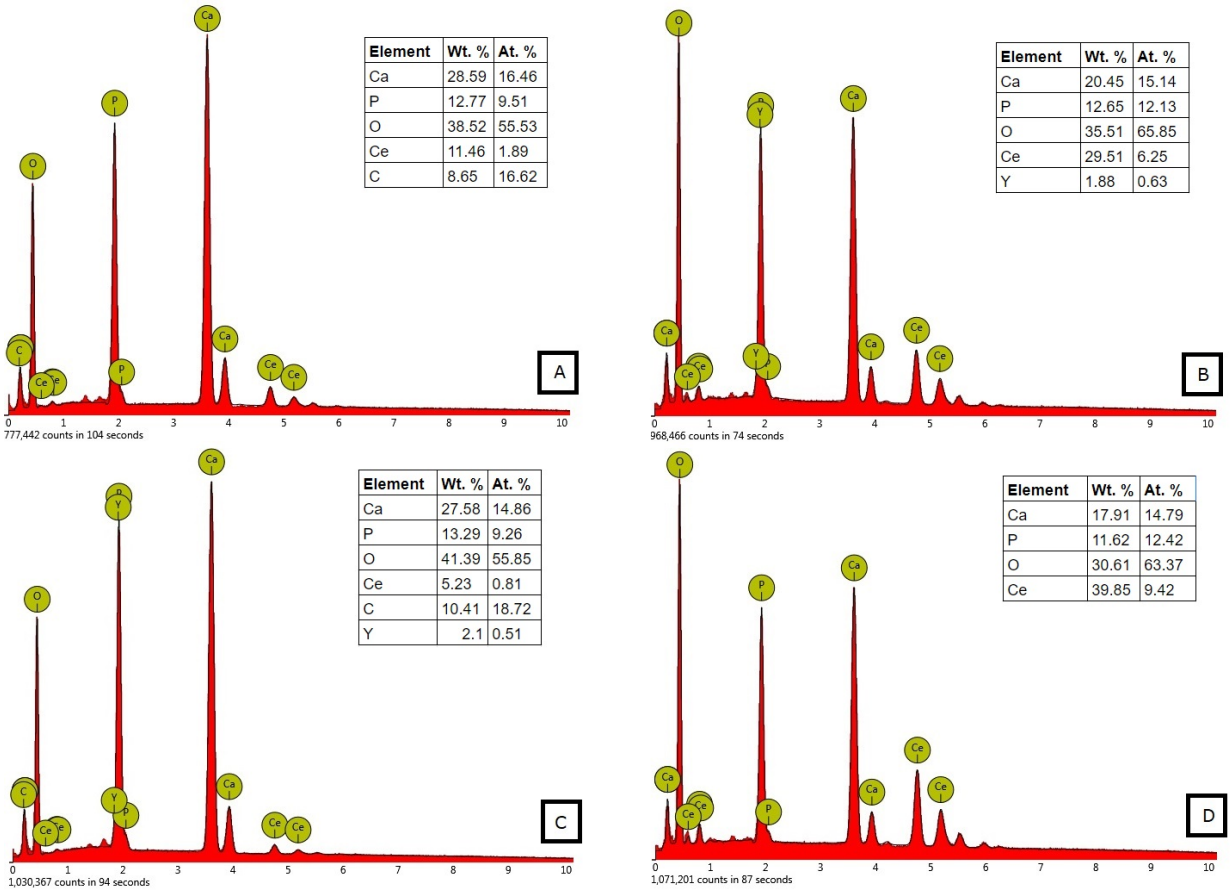


Figure 4.14: EDS analysis of samples A) 10% CeHAp at 400ºC, B) 20% CeHAp at 400 ºC, C) 10% CeHAp at 800ºC, D) 20% CeHAp at 800 ºC

## 4.2 Optical Characterization

Here will be developed an optical analysis of the samples through UV-Vis Spectroscopy and Fluorescence Microscopy to obtain band gap, absorbance, and fluorescence related information of the synthesized material.

### 4.2.1 UV-Vis Spectroscopy Analysis

**Diffuse Reflectance analysis**

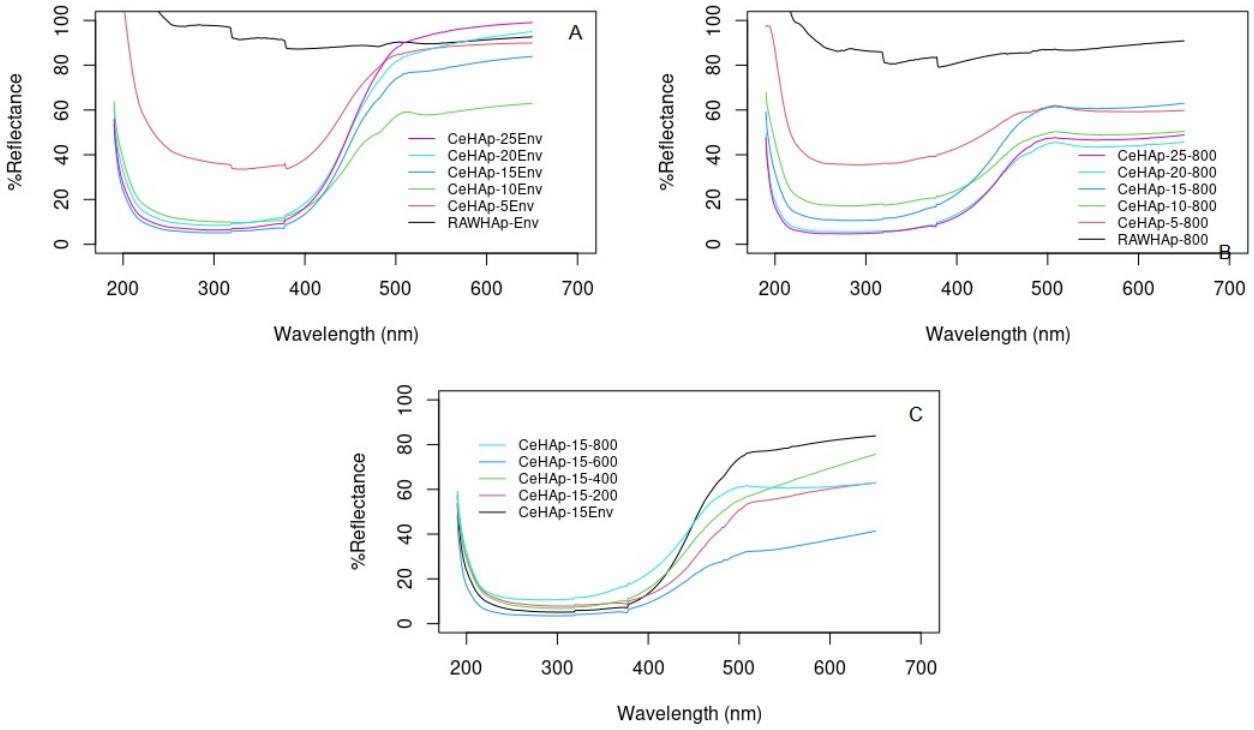


Figure 4.15: Diffuse Reflectance graphs for a) Environmental batch samples b) Samples at 800 ºC and C) 15% samples submitted to all temperatures.

Diffuse reflectance percentage was measured for all the samples. The spectra emission is related to the optical response of the cerium nanoparticles that substituted the calcium ions in HAp. Spectra displayed in figure 4.15, produce a response in the region between 300 nm and 400 nm with a maximum at approximately 360 nm according to the literature. The intensity increases with the raising concentration of Ce ions and is not affected by temperature. The presence of Ce ions can lead to changes in the optical properties of the material, affecting its absorbance and reflectance properties. Ce ions can introduce new energy levels and electronic transitions in the material. Additionally, the presence of this ions affects the crystal structure and the morphology of the material, affecting its refractive index and scattering process. The diffuse reflectance of the material can be affected by the presence of Ce

ions due to the overlap between their electronic transitions and the absorption spectra of the HAp material.

### Energy band gap analysis

Energy band gap ($E_g$) for all the samples at the different temperatures were calculated using diffuse reflectance experiments. Using Kubelka-Munk model for the estimation of the absorption coefficient as performed in the literature, using the following equation:

$$F(R) = \frac{K}{S} = \frac{(1-R)^2}{R} \approx \alpha \tag{4.1}$$

where, F(R) stands for the Kubelka-Munk function, K represents the absortion coefficient and S is the scattering coefficient while R reflectance is equal to: $R_{sample}/R_{standard}$. This expression is proportional to the absorption coefficient ($\alpha$)[89]. Band gap estimation was performed using Tauc Plot taking into account allowed indirect and direct optical transition. The modified Tauc equation used for obtaining the calculations is:

$$h\nu F(R) = A * (h\nu - E_g)^{\gamma} \tag{4.2}$$

with $\gamma$= 1/2 for the direct case and $\gamma$= 2 for the indirect one[90]. $E_g$ can be obtained by ploting $[F(R)h\nu]^{1/2}$ against the product of hv, taking the tangent line of the curve an saving the intercepting point in the x-axis. All band gap values calculated are available in Table 4.2.

### Band Gap Calculations Diffuse Reflectance

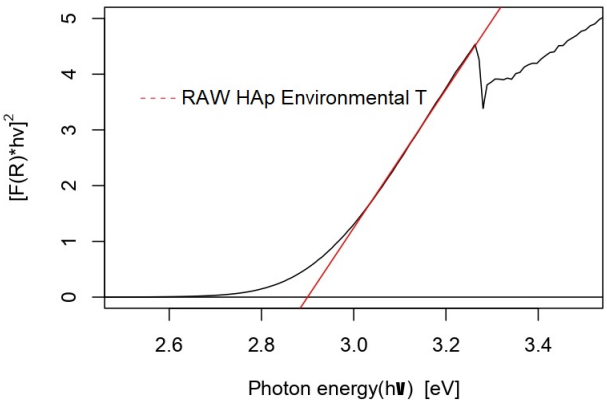


Figure 4.16: RAW HAp band gap calculation with y = 2.

$E_g$ band gap energy values, obtained as shown in figures 4.16 and 4.17, are in the range of 2.04 to 2.62 for the direct calculations, meanwhile for the indirect calculations, the values oscillate in the zone between 2.80 and 3.02. In table

4.2, all data corresponding to each sample is showed.

Other works have reported a $E_g$ value for the Hydroxyapatite with values of 3.45 eV to 5.78 eV[91 92]. Indirect electronic transition process is going to be assumed for the progression of the discussion. Differences in theoretical and experimental values can be assumed as product of the increasing defects density in the lattice due to different conditions variation during the synthesis process or the received temperature hits provided to the samples. Data shows a reduction in the value of the band gap with dopant increasing value. The reported value of $E_g$ for cerium oxide nanoparticles is approximately 2.3 eV[93 94].

It can be induced that the band gap values of substituted samples is shifting torwards the value of cerium nanoparticles itself that can be explained as a new band width of a certain new composite.

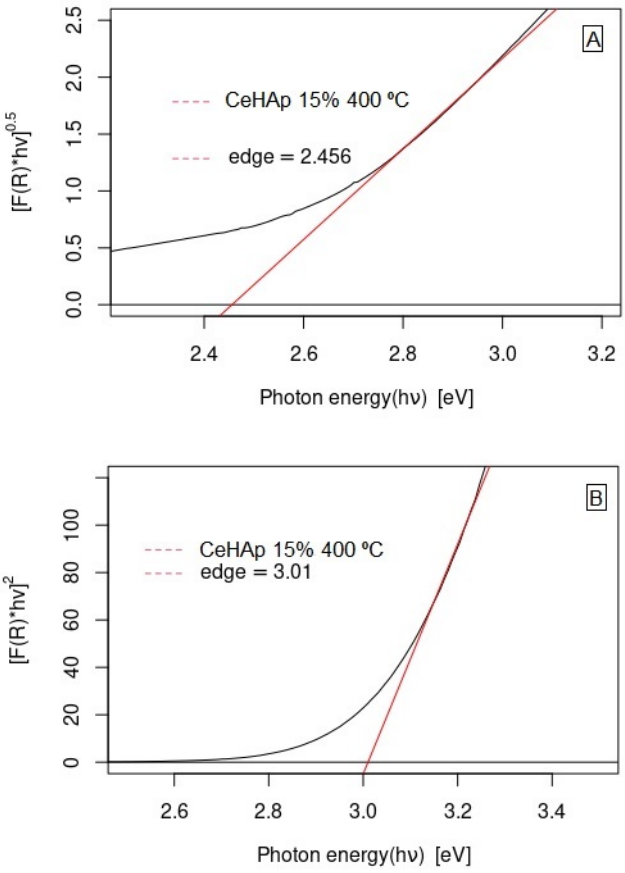


Figure 4.17: Tauc plot for obtaining estimated band gap values. A) Direct method for 15% CeHAp at 400ºC and B) Indirect method for 15% CeHAp at 400ºC

| **$E_g$ values** | | | | |
|---|---|---|---|---|
| Samples | [Ce] (mmol) | Temperature | Direct ($\gamma$= 1/2) | Indirect ($\gamma$= 2) |
| Raw HAp | 0 | 25 | - | - |
| $Ce_{0.5}$-HAp | 0.5 | 25 | 2.53 | 2.91 |
| $Ce_1$-HAp | 1 | 25 | 2.47 | 2.95 |
| $Ce_{1.5}$-HAp | 1.5 | 25 | 2.62 | 3.02 |
| $Ce_2$-HAp | 2 | 25 | 2.59 | 2.99 |
| $Ce_{2.5}$-HAp | 2.5 | 25 | 2.62 | 3.01 |
| Raw HAp | 0 | 200 | - | - |
| $Ce_{0.5}$-HAp | 0.5 | 200 | 2.42 | 2.88 |
| $Ce_1$-HAp | 1 | 200 | 2.40 | 2.92 |
| $Ce_{1.5}$-HAp | 1.5 | 200 | 2.52 | 2.97 |
| $Ce_2$-HAp | 2 | 200 | 2.49 | 2.95 |
| $Ce_{2.5}$-HAp | 2.5 | 200 | 2.46 | 2.96 |
| Raw HAp | 0 | 400 | - | - |
| $Ce_{0.5}$-HAp | 0.5 | 400 | 2.31 | 2.87 |
| $Ce_1$-HAp | 1 | 400 | 2.26 | 2.89 |
| $Ce_{1.5}$-HAp | 1.5 | 400 | 2.46 | 3.01 |
| $Ce_2$-HAp | 2 | 400 | 2.49 | 2.01 |
| $Ce_{2.5}$-HAp | 2.5 | 400 | 2.38 | 2.97 |
| Raw HAp | 0 | 600 | - | - |
| $Ce_{0.5}$-HAp | 0.5 | 600 | 2.39 | 2.96 |
| $Ce_1$-HAp | 1 | 600 | 2.38 | 2.97 |
| $Ce_{1.5}$-HAp | 1.5 | 600 | 2.41 | 2.99 |
| $Ce_2$-HAp | 2 | 600 | 2.58 | 3.03 |
| $Ce_{2.5}$-HAp | 2.5 | 600 | 2.49 | 3.00 |
| Raw HAp | 0 | 800 | - | - |
| $Ce_{0.5}$-HAp | 0.5 | 800 | 2.04 | 2.80 |
| $Ce_1$-HAp | 1 | 800 | 2.22 | 2.85 |
| $Ce_{1.5}$-HAp | 1.5 | 800 | 2.44 | 2.98 |
| $Ce_2$-HAp | 2 | 800 | 2.43 | 2.99 |
| $Ce_{2.5}$-HAp | 2.5 | 800 | 2.46 | 2.98 |

Table 4.2: Sample preparation of HAp doped with different concentrations of Cerium

### 4.2.2 Fluorescence Microscopy

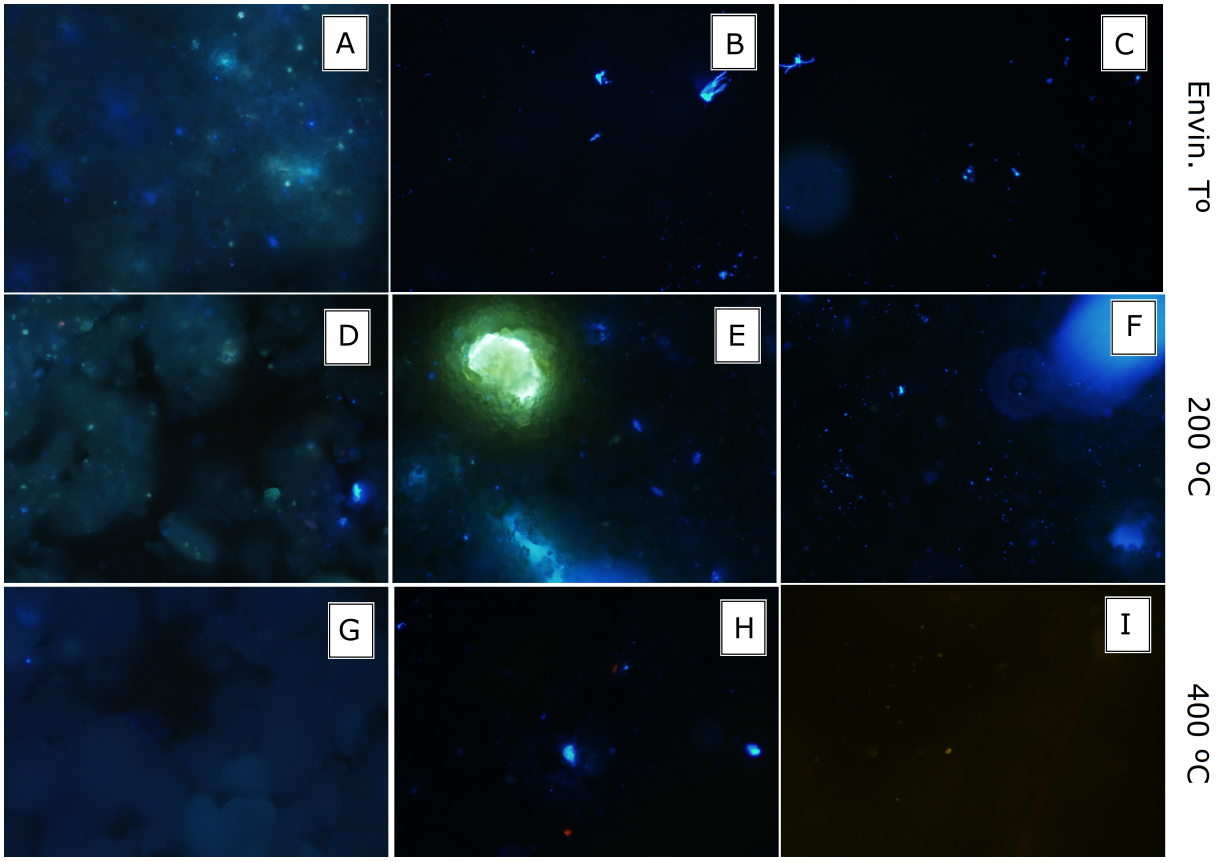


Figure 4.18: Fluorescence response of HAp and CeHAp samples at Environmental, 200 ºC and 600 ºC. From left to right in each line, A), D) and G) are RAW Samples . B), E) and H) are 10% samples. C), F) and I) are with 20% dopant content.

Fluorescence response shown in figure 4.18 is present in natural hydroxyapatite samples at room temperature and after heat treatment at 200 ºC and 400 ºC. The addition of the cerium nanoparticles did not increment the response using the blue filter in the microscope. This can be attributed to the excitation source as the wavelength needed to obtain optical responses of Cerium nanoparticles is in the zone of 290 nm to 350 nm, as reported in previous works and in accordance to the absorbance obtained in the UV-Vis analysis. When samples were calcined at 600 ºC (figure 4.19), the same response in pure samples was acquired. Some particles react when the concentration of foreign ions reaches 10%, nevertheless until the 20% level, a high response was obtained with either the blue or green filter. At 800 ºC, HAp changes the color in the response of the particles providing a red color response as shown in figure 4.20. This shift could be due to the crystal structure change suggested by XRD, FTIR, and Raman spectrums.

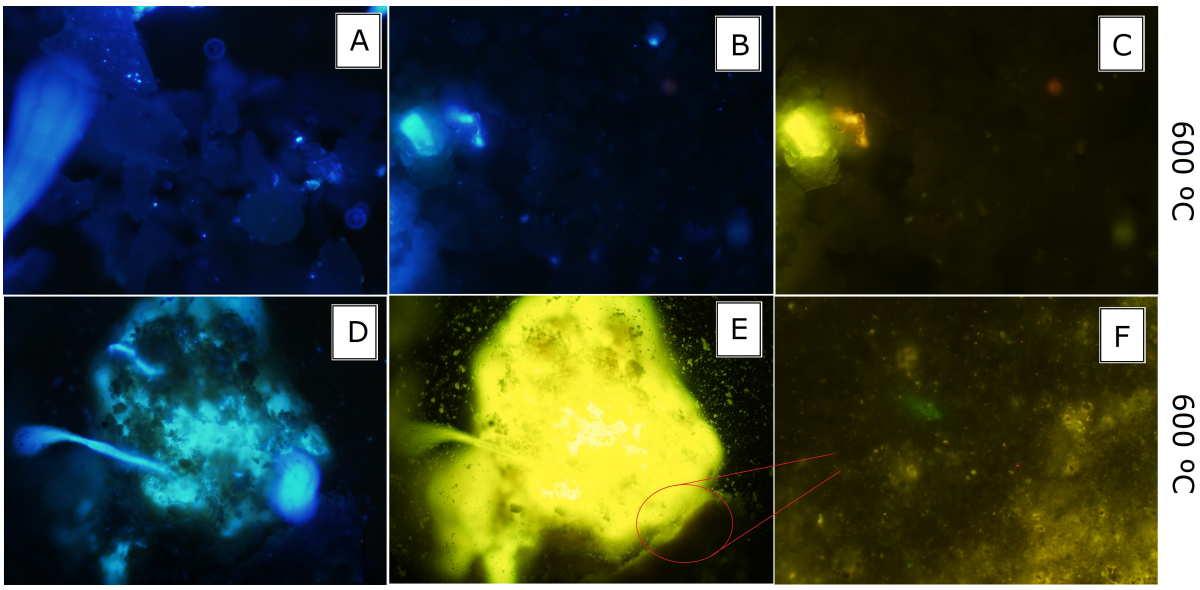


Figure 4.19: Fluorescence response of HAp and CeHAp samples at 600 ºC. A) is RAW HAp, B) is 10% sample with blue filter and C) with green filter. D) corresponds to 20% samples with blue filter, E) with green filter and F) is the augmented zone of the response.

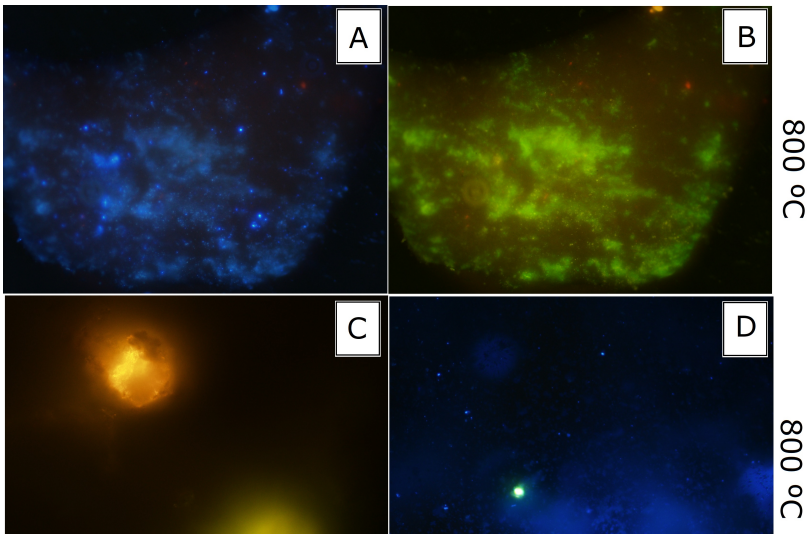


Figure 4.20: Fluorescence response of HAp and CeHAp samples at 800 ºC. A) is RAW HAp with blue filter, B) with green filter. C) is 10% cerium HAp and D) corresponds to 20% samples with blue filter.

### 4.2.3 Final Discussion

The results obtained by the structural characterization suggest that a pure form of HAp was obtained. In addition, cerium ions were successfully introduced to the lattice of HAp as FTIR, XRD, and Raman spectra evidenced its vibrational modes. SEM imaging allowed the visualization of the nanocomposite exhibiting the well dispersed cerium in the structure with crystal agglomerations and irregular morphology. The concentration of the dopant influences the particle size as it can lead to the formation of smaller particles due to the effect of the foreign ions on the nucleation and growth rates during the synthesis process. Temperature may also contribute to the acceleration of the nucleation and growth rates while it produces sharper particles. FTIR spectra described that the substitution process was carried out successfully as well as XRD patterns at low temperatures, but with the increase of temperature (> 600ªC) the foreign ions start to act as dopant in the structure producing changes that was noted with the peaks of the techniques mentioned above and corroborated with the fluorescence microscopy which changed its emission form a yellow-green color to a red one. EDS analysis showed the atomic composition of the samples, revealing Ca, P, O, and Ce peaks in Ce-HAp samples. UV-Vis spectroscopy with diffuse reflectance method was used to obtain a reflectance graph showing the optical properties of the materials with peaks in the region of 300 nm to 400 nm which is related to the introduction of new energy levels and electronic transitions in the material. It also was employed to calculate the energy band gaps of the samples that decrease their width with the addition of Ce ions. Finally, fluorescence microscopy revealed the fluorescence response of Raw HAp as light blue that, when reaching 800 ºC, shifts to a red response. A high response was obtained by samples with equal or over 20% of Ce ions at 600 ºC, even with a higher excitation wavelength than the recommended. This is related to the results of the UV-Vis analysis as the diminishing in band gap with the high number of cerium ions led to a response even when the wavelength did not match the requirements.

The potential applications the material can exhibit are due to the capability of Ce ions to scavenge free radicals and regulate the immune system which leads to its antibacterial, anti-inflammatory and antioxidant properties[95]. The antioxidant properties of Ce ions are due to the ability to undergo redox cycles between Ce (III) and Ce(IV) states, which allows them to scavenge free radicals suchs peroxide, hydroxyl or nitric oxide. Ce ions can act as a catalytic antioxidant by donating or accepting electrons to neutralize free radicals and prevent further damage to cellular components such as lipids, proteins and DNA[96]. Ce ions have also shown to have anti-inflammatory effects by regulating the immune response. Ce ions can modulate the production of cytokines and chemokines, which are signaling molecules involved in the recruitment and activation of immune cells. Ce ions have been shown to reduce the production of pro-inflammatory cytokines such as interleukin-1(1L - 1), interleukin-6 (1L - 6), and tumor necrosis factor-α(TNF-α), while increasing the production of anti-inflammatory cytokines such as interleukin-10 (IL-10)[97 98]. Antibacterial properties are also attributed to their ability to scavenge free radicals and regulate the immune system as mentioned before. Ce ions cans disrupt bacterial membranes and inhibit bacterial growth by generating ROS such as the ones the ones mentioned earlier in this section. Ce ions can also modulate the expression of virulence factors and enhance the phagocyte activity of immune cells such as macrophages[98 99]. The antibacterial, antioxidant and anti-inflammatory properties of CeHAp samples dependent on their concentration and redox state, as well as the local micro environment. At low concentrations, Ce ions can exhibit antioxidant and anti-inflammatory effects, while at high concentrations, they may have pro-oxidant and pro-inflammatory effects, which can be used in the

biomedical field to stimulate immune responses and to fight against cancerous cells, or in energy-related applications where it can be used as additives in fuel cells and batteries to improve their performance [100]. The precise mechanism by which Ce ions exert their biological properties in CeHAp samples are still a subject of ongoing research.

Optical properties of the developed CeHAp material can also provide applications in the some fields such as acting as a contrast agent in biomedical imaging due to its fluorescence and luminescence properties, it can also be use for drug delivery systems where it can be used as a drug carrier due to its surface area and biocompatibility, where the properties mentioned can be used to track the system in real-time [66 67]. The material can also act as biosensors where CeHAp can be used as a sensing material for various analytes due to its sensitivity towards changes in temperature, pressure, and chemical environment. The luminescent properties can help in detecting and quantifying the analytes with high accuracy [101 100]. In addition, the material can be used also as a photocatalyst due to its ability to absorb light in the UV and visible regions, where the optical properties can help promoting the generation of ROS and OH radicals that can degrade pollutants and contaminants in the environment [102]. Finally, the material can be used in optoelectronic devices such as light-emitting diodes and solar cells due to its ability to emit light and absorb photons, improving the efficiency and performance of these devices [103].

# Chapter 5

# Conclusions & Outlook

The current project reports the synthesis of hydroxyapatite and cerium substituted HAp samples using the hydrothermal method. Characterization methods (SEM, FTIR Spectroscopy, XRD, EDS, and Raman spectroscopy) confirmed that the ionic substitution that led into a doped CeHAp did took place in the reaction the cerium nanoparticles in the system. FTIR and XRD spectroscopy revealed the vibrational modes of the constituents groups ($OH^-$ and $PO_4^{3+}$) of HAp in addition to the carbonate groups product of the direct contact of the samples with $CO_2$ present in the air. Samples with high cerium content (> 20%) at high temperatures (over 600ºC) revealed possible crystal structure change in the apatite host. Raman spectroscopy corroborated the obtained information from the structural analysis made on the samples. SEM microscopy revealed well dispersed cerium in the samples with irregular morphology with crystal agglomerations. When the level of foreign ions is increased, smaller size of particles can be distinguished in the micrographs. Temperature helps the formation of better defined shapes in the particles and also favors the reduction of the particle size. EDS analysis revealed the composition of the samples with the presence of Ca, O, Ce, and P related peaks. UV-Vis spectroscopy was employed to obtain diffuse reflectance spectrums related to the sample´s optical response that increases with the concentration of substituent. In addition, the method was used to obtain estimated band gap values for the samples in the direct and indirect form, observing a diminishing width of the band with the concentration related to increasing defects in the material. Fluorescence spectroscopy showed the intrinsic emission of the response in RAW samples with a higher response at a concentration percentage of 20% submitted to 600 ºC for one hour. Other samples revealed a weak emission related to the missmatch in the excitation wavelength available for the analysis and the ones theoretically proposed.

In conclusion, a successful method for the development of CeHAp material was applied, with variation in the Ce ions concentration and taking into account the temperature factor during the synthesis. Results suggest that at environmental and relative lower temperatures, the Ce ions entered the hydroxylated apatite without changing the structural behavior of the samples. In addition to high concentration levels of substituent, it act as a dopant where the material shifts to a different crystal structure when submitted to high temperatures. This change can also be seen with the fluorescent response that goes from light blue to reddish. Hydroxyapatite applications in the biomedical field as imaging component or host as drug delivery carrier, when ion added with antibacterial properties or enhanced

mechanical and optical characteristics are continuously in development

.

This work can be complemented with biomedical studies related to antibacterial responses as well as biocompatibility analysis for safe applications. Less spaced concentration variation as well as temperature changes can help into improving the analysis of materials. Finally, this novel compounds can be used to perform drug delivery systems, biosensors, antibacterial, antioxidant and anti-inflammatory applications.

# Appendix A

# Long Appendix 1 Heading

### A.0.1 FTIR spectra

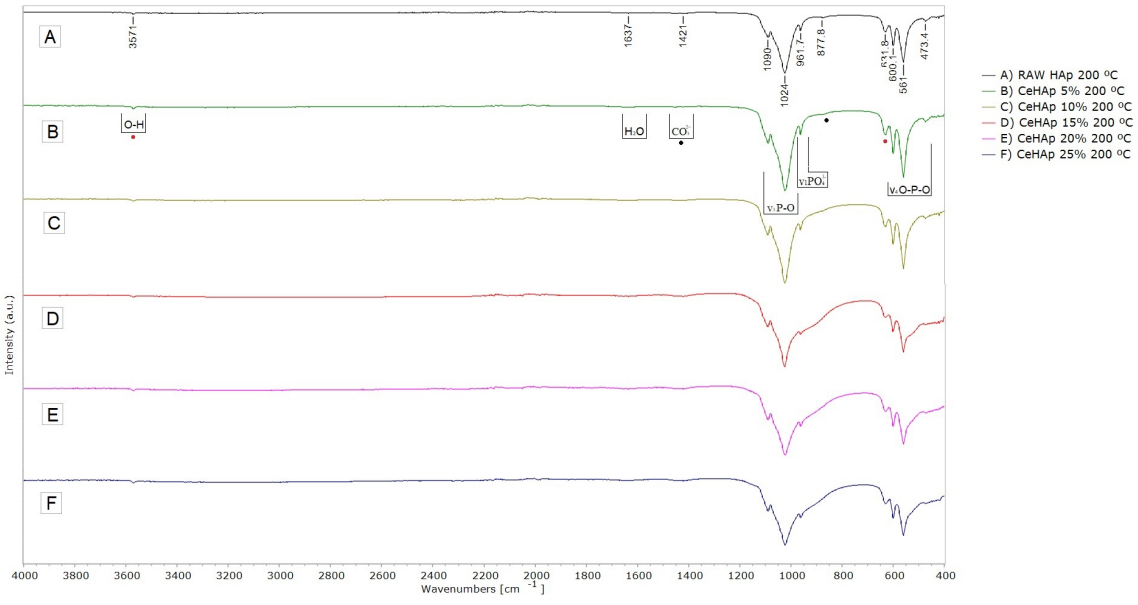


Figure A.1: FTIR spectra of samples submitted to 200 ºC. a) Raw HAp, b) 5% CeHAp, c) 10% CeHAp, d) 15% CeHAp, e) 20% CeHAp and f) 25% CeHAp.

### A.0.2 XRD patterns

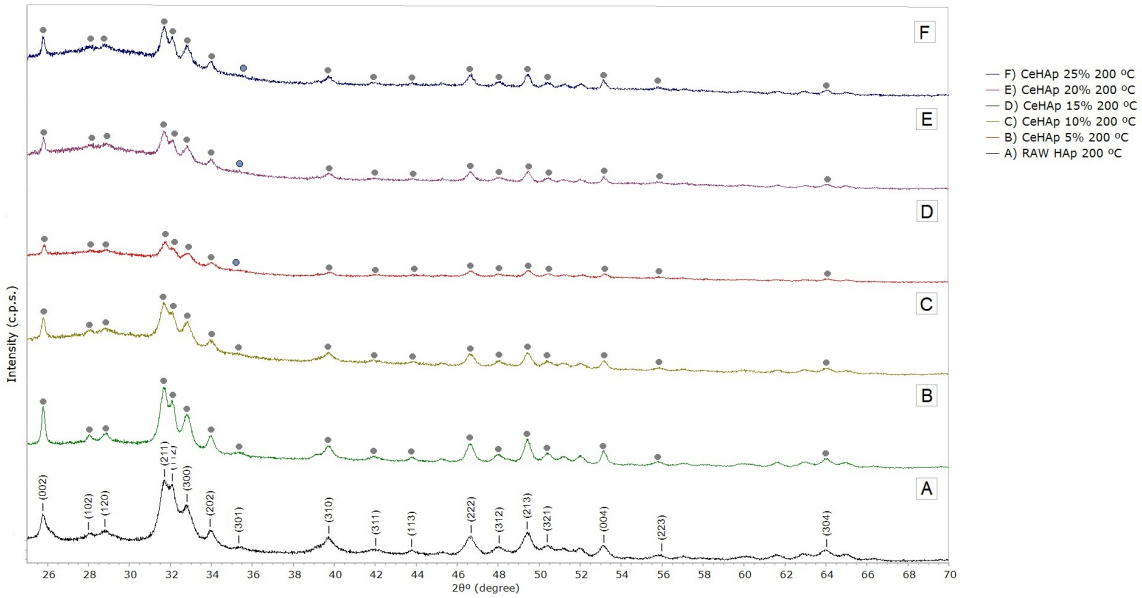


Figure A.2: XRD patterns of samples submitted to 200 ºC. a) Raw HAp, b) 5% CeHAp, c) 10% CeHAp, d) 15% CeHAp, e) 20% CeHAp and f) 25% CeHAp.

### A.0.3 Raman patterns

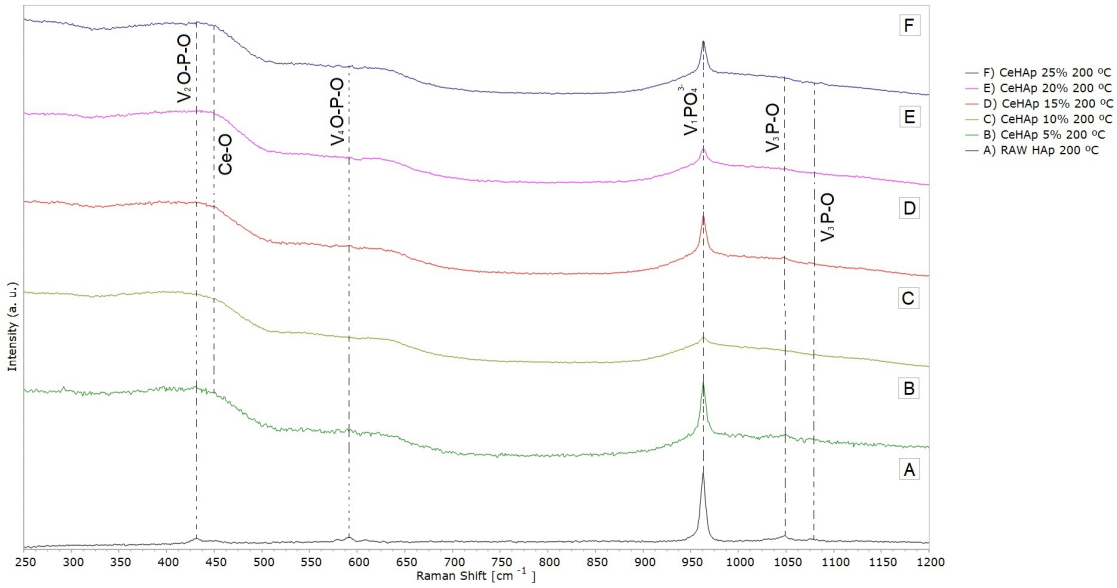


Figure A.3: Raman spectra of samples submitted to 200 ºC. a) Raw HAp, b) 5% CeHAp, c) 10% CeHAp, d) 15% CeHAp, e) 20% CeHAp and f) 25% CeHAp.

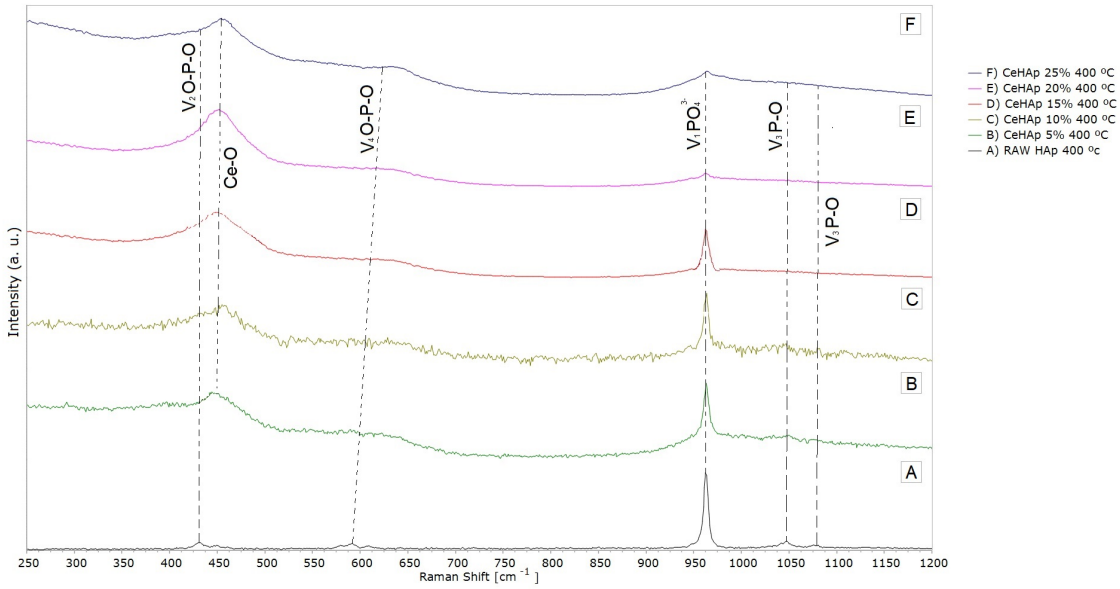


Figure A.4: Raman spectra of samples submitted to 400 ºC. a) Raw HAp, b) 5% CeHAp, c) 10% CeHAp, d) 15% CeHAp, e) 20% CeHAp and f) 25% CeHAp.

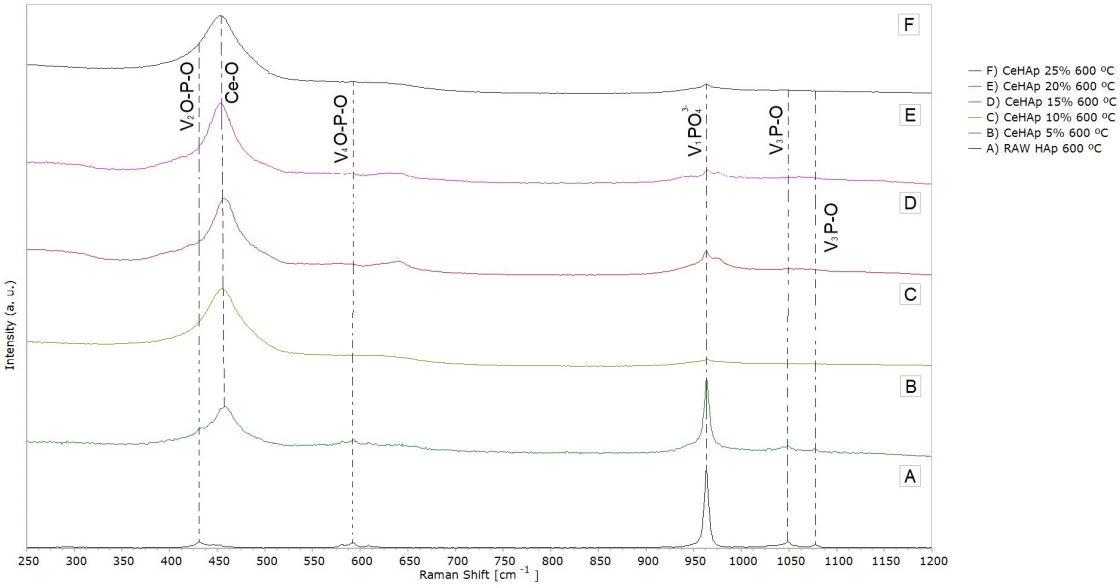


Figure A.5: Raman Spectra of samples submitted to 600 ºC. a) Raw HAp, b) 5% CeHAp, c) 10% CeHAp, d) 15% CeHAp, e) 20% CeHAp and f) 25% CeHAp.

# Bibliography


[1] Deshpande, S.; Patil, S.; Kuchibhatla, S. V.; Seal, S. Size dependency variation in lattice parameter and valency states in nanocrystalline cerium oxide. *Applied Physics Letters* **2005**, *87*, 133113.

[2] Wolf, D. E. Fundamentals of fluorescence and fluorescence microscopy. *Methods in cell biology* **2003**, *72*, 157–184.

[3] Machado, T. R.; Sczancoski, J. C.; Beltran-Mir, H.; Li, M. S.; Andres, J.; Cordoncillo, E.; Leite, E.; Longo, E. Structural properties and self-activated photoluminescence emissions in hydroxyapatite with distinct particle shapes. *Ceramics International* **2018**, *44*, 236–245.

[4] Gonzalez, G.; Costa-Vera, C.; Borrero, L. J.; Soto, D.; Lozada, L.; Chango, J. I.; Diaz, J. C.; Lascano, L. Effect of carbonates on hydroxyapatite self-activated photoluminescence response. *Journal of Luminescence* **2018**, *195*, 385–395.

[5] Perkowitz, S. *Optical characterization of semiconductors: infrared, Raman, and photoluminescence spectroscopy*; Elsevier, 2012.

[6] Rostron, P.; Gaber, S.; Gaber, D. Raman spectroscopy, review. *laser* **2016**, *21*, 24.

[7] Mezzetti, A.; Leibl, W. Time-resolved infrared spectroscopy in the study of photosynthetic systems. *Photosynthesis Research* **2017**, *131*, 121–144.

[8] Leng, Y. *Materials characterization: introduction to microscopic and spectroscopic methods*; John Wiley & Sons, 2009.

[9] Song, N.; Wang, A.-j.; Li, J.-m.; Zhu, Z.; Shi, H.; Ma, X.-l.; Sun, D. Study on influencing factors of Pickering emulsions stabilized by hydroxyapatite nanoparticles with nonionic surfactants. *Soft Matter* **2018**, *14*, 3889–3901.

[10] Gohain, N. Studies on the structure and function of phenazine modifying enzymes PhzM and PhzS involved in the biosynthesis of pyocyanin. Ph.D. thesis, 2009.

[11] Maier, A.; Steidl, S.; Christlein, V.; Hornegger, J. Medical imaging systems: An introductory guide. **2018**,

[12] Freitas, R. A. *Nanomedicine, volume I: basic capabilities*; Landes Bioscience Georgetown, TX, 1999; Vol. 1.

[13] Leary, J. F. *Fundamentals of Nanomedicine*; Cambridge University Press, 2022.

[14] Duschl, A. *Immune Rebalancing*; Elsevier, 2016; pp 251–274.

[15] Neacsu, I. A.; Stoica, A. E.; Vasile, B. S.; Andronescu, E. Luminescent hydroxyapatite doped with rare earth elements for biomedical applications. *Nanomaterials* **2019**, *9*, 239.

[16] Honda, Y.; Anada, T.; Morimoto, S.; Shiwaku, Y.; Suzuki, O. Effect of Zn2+ on the physicochemical characteristics of octacalcium phosphate and its hydrolysis into apatitic phases. *Crystal growth & design* **2011**, *11*, 1462–1468.

[17] Tavakol, S.; Nikpour, M. R.; Hoveizi, E.; Tavakol, B.; Rezayat, S. M.; Adabi, M.; Shajari Abokheili, S.; Jahanshahi, M. Investigating the effects of particle size and chemical structure on cytotoxicity and bacteriostatic potential of nano hydroxyapatite/chitosan/silica and nano hydroxyapatite/chitosan/silver; as antibacterial bone substitutes. *Journal of nanoparticle research* **2014**, *16*, 1–13.

[18] Palard, M.; Balencie, J.; Maguer, A.; Hochepied, J.-F. Effect of hydrothermal ripening on the photoluminescence properties of pure and doped cerium oxide nanoparticles. *Materials Chemistry and Physics* **2010**, *120*, 79–88.

[19] Hajjiah, A.; Samir, E.; Shehata, N.; Salah, M. Lanthanide-Doped Ceria Nanoparticles as Backside Coaters to Improve Silicon Solar Cell Efficiency. *Nanomaterials* **2018**, *8*, 357.

[20] White, A. A.; Best, S. M.; Kinloch, I. A. Hydroxyapatite–carbon nanotube composites for biomedical applications: a review. *International Journal of Applied Ceramic Technology* **2007**, *4*, 1–13.

[21] Gomes, D. S.; Santos, A. M.; Neves, G. A.; Menezes, R. R. A brief review on hydroxyapatite production and use in biomedicine. *Cerâmica* **2019**, *65*, 282–302.

[22] Tank, K. P.; Chudasama, K. S.; Thaker, V. S.; Joshi, M. J. Pure and zinc doped nano-hydroxyapatite: Synthesis, characterization, antimicrobial and hemolytic studies. *Journal of Crystal Growth* **2014**, *401*, 474–479.

[23] Hench, L. *An introduction to bioceramics, second edition*; 2013; pp 1–600.

[24] Murugan, R.; Ramakrishna, S. Development of nanocomposites for bone grafting. *Composites Science and technology* **2005**, *65*, 2385–2406.

[25] Hughes, J. M.; Rakovan, J. The Crystal Structure of Apatite, Ca5(PO4)3(F,OH,Cl). *Reviews in Mineralogy and Geochemistry* **2002**, *48*, 1–12.

[26] Eliaz, N.; Metoki, N. Calcium Phosphate Bioceramics: A Review of Their History, Structure, Properties, Coating Technologies and Biomedical Applications. *Materials* **2017**, *10*, 334.

[27] Güler, H.; Gündoğmaz, G.; Kurtuluş, F.; Çelik, G.; Gacanoğlu, Ş. Solid state synthesis of calcium borohydroxyapatite. *Solid State Sciences* **2011**, *13*, 1916–1920.

[28] Pu'ad, N. M.; Koshy, P.; Abdullah, H.; Idris, M.; Lee, T. Syntheses of hydroxyapatite from natural sources. *Heliyon* **2019**, *5*, e01588.

[29] Ghosh, R.; Sarkar, R. Synthesis and characterization of sintered hydroxyapatite: a comparative study on the effect of preparation route. *Journal of the Australian Ceramic Society* **2018**, *54*, 71–80.

[30] Nazeer, M. A.; Yilgor, E.; Yagci, M. B.; Unal, U.; Yilgor, I. Effect of reaction solvent on hydroxyapatite synthesis in sol–gel process. *Royal Society open science* **2017**, *4*, 171098.

[31] Castro, M. A. M.; Oliveira, T. P.; Correia, G. S.; Oliveira, M. M.; Rangel, J. H. G.; Rodrigues, S. F.; Mercury, J. M. R. Synthesis of hydroxyapatite by hydrothermal and microwave irradiation methods from biogenic calcium source varying pH and synthesis time. *Boletín de la Sociedad Española de Cerámica y Vidrio* **2020**,

[32] Ortiz, G. M. H.; Parra, R.; Fanovich, M. A. Comparative hydrothermal synthesis of hydroxyapatite by using cetyltrimethylammonium bromide and hexamethylenetetramine as additives. *Ceramics International* **2018**, *44*, 3658–3663.

[33] Edralin, E. J. M.; Garcia, J. L.; dela Rosa, F. M.; Punzalan, E. R. Sonochemical synthesis, characterization and photocatalytic properties of hydroxyapatite nano-rods derived from mussel shells. *Materials Letters* **2017**, *196*, 33–36.

[34] Kaygili, O.; Keser, S.; Bulut, N.; Ates, T. Characterization of Mg-containing hydroxyapatites synthesized by combustion method. *Physica B: Condensed Matter* **2018**, *537*, 63–67.

[35] Cho, J. S.; Lee, J.-C.; Rhee, S.-H. Effect of precursor concentration and spray pyrolysis temperature upon hydroxyapatite particle size and density. *Journal of Biomedical Materials Research Part B: Applied Biomaterials* **2016**, *104*, 422–430.

[36] Milovac, D.; Ferrer, G. G.; Ivankovic, M.; Ivankovic, H. PCL-coated hydroxyapatite scaffold derived from cuttlefish bone: Morphology, mechanical properties and bioactivity. *Materials Science and Engineering: C* **2014**, *34*, 437–445.

[37] Goloshchapov, D.; Kashkarov, V.; Rumyantseva, N.; Seredin, P.; Lenshin, A.; Agapov, B.; Domashevskaya, E. Synthesis of nanocrystalline hydroxyapatite by precipitation using hen's eggshell. *ceramics International* **2013**, *39*, 4539–4549.

[38] Türk, S.; Altınsoy, İ.; ÇelebiEfe, G.; İpek, M.; Özacar, M.; Bindal, C. Microwave–assisted biomimetic synthesis of hydroxyapatite using different sources of calcium. *Materials Science and Engineering: C* **2017**, *76*, 528–535.

[39] Holopainen, J.; Ritala, M. Rapid production of bioactive hydroxyapatite fibers via electroblowing. *Journal of the European Ceramic Society* **2016**, *36*, 3219–3224.

[40] others,, *et al.* Substituents and dopants in the structure of apatite. *Apatites and their synthetic analogues—synthesis, structure, properties and applications. InTech, Open Acces monograph* **2016**, 289–334.

[41] Ciobanu, G.; Bargan, A. M.; Luca, C. New cerium (IV)-substituted hydroxyapatite nanoparticles: Preparation and characterization. *Ceramics International* **2015**, *41*, 12192–12201.

[42] Cockbain, A. The crystal chemistry of the apatites. *Mineralogical magazine and journal of the Mineralogical Society* **1968**, *36*, 654–660.

[43] Cockbain, A.; Smith, G. Alkaline-earth-rare-earth silicate and germanate apatites. *Mineralogical magazine and journal of the Mineralogical Society* **1967**, *36*, 411–421.

[44] Zhang, F.; Wang, P.; Koberstein, J.; Khalid, S.; Chan, S.-W. Cerium oxidation state in ceria nanoparticles studied with X-ray photoelectron spectroscopy and absorption near edge spectroscopy. *Surface Science* **2004**, *563*, 74–82.

[45] Mogensen, M.; Sammes, N. M.; Tompsett, G. A. Physical, chemical and electrochemical properties of pure and doped ceria. *Solid state ionics* **2000**, *129*, 63–94.

[46] Rzigalinski, B. A.; Meehan, K.; Davis, R. M.; Xu, Y.; Miles, W. C.; Cohen, C. A. Radical nanomedicine. **2006**,

[47] Tsunekawa, S.; Fukuda, T.; Kasuya, A. Blue shift in ultraviolet absorption spectra of monodisperse CeO 2- x nanoparticles. *Journal of Applied Physics* **2000**, *87*, 1318–1321.

[48] others,, *et al.* Neuroprotective mechanisms of cerium oxide nanoparticles in a mouse hippocampal brain slice model of ischemia. *Free Radical Biology and Medicine* **2011**, *51*, 1155–1163.

[49] Deus, R.; Cortés, J.; Ramirez, M.; Ponce, M.; Andres, J.; Rocha, L.; Longo, E.; Simões, A. Photoluminescence properties of cerium oxide nanoparticles as a function of lanthanum content. *Materials Research Bulletin* **2015**, *70*, 416–423.

[50] Murthy, K.; Virk, H. S. Luminescence phenomena: an introduction. **2014**, *347*, 1–34.

[51] Kumar, G. S.; Girija, E. Flower-like hydroxyapatite nanostructure obtained from eggshell: A candidate for biomedical applications. *Ceramics International* **2013**, *39*, 8293–8299.

[52] Lijuan, X.; Liuyun, J.; Chengdong, X.; Lixin, J. Effect of different synthesis conditions on the microstructure, crystallinity and solubility of Mg-substituted hydroxyapatite nanopowder. *Advanced Powder Technology* **2014**, *25*, 1142–1146.

[53] Tanaka, H.; Ohnishi, A. Synthesis of Ti (IV)-substituted calcium hydroxyapatite microparticles by hydrolysis of phenyl phosphates. *Advanced Powder Technology* **2013**, *24*, 1028–1033.

[54] Uskoković, V. The role of hydroxyl channel in defining selected physicochemical peculiarities exhibited by hydroxyapatite. *RSC advances* **2015**, *5*, 36614–36633.

[55] Botelho, G.; Sczancoski, J. C.; Andres, J.; Gracia, L.; Longo, E. Experimental and theoretical study on the structure, optical properties, and growth of metallic silver nanostructures in Ag3PO4. *The Journal of Physical Chemistry C* **2015**, *119*, 6293–6306.

[56] Arul, K. T.; Ramya, J. R.; Kalkura, S. N. *Biomaterials*; IntechOpen, 2020.

[57] Arul, K. T.; Ramya, J. R.; Bhalerao, G.; Kalkura, S. N. Physicochemical characterization of the superhydrophilic, magnesium and silver ions co-incorporated nanocrystalline hydroxyapatite, synthesized by microwave processing. *Ceramics International* **2014**, *40*, 13771–13779.

[58] Popa, C.; Ciobanu, C. Synthesis and characterization of fluorescent hydroxyapatite. *Rom. Rep. Phys* **2016**, *68*, 1170–1177.

[59] Alshemary, A. Z.; Akram, M.; Goh, Y.-F.; Kadir, M. R. A.; Abdolahi, A.; Hussain, R. Structural characterization, optical properties and in vitro bioactivity of mesoporous erbium-doped hydroxyapatite. *Journal of Alloys and Compounds* **2015**, *645*, 478–486.

[60] Feng, Z.; Liao, Y.; Ye, M. Synthesis and structure of cerium-substituted hydroxyapatite. *Journal of materials science: materials in medicine* **2005**, *16*, 417–421.

[61] Zhang, Q.; Yang, X.; Deng, R.; Zhou, L.; Yu, Y.; Li, Y. Synthesis and near infrared luminescence properties of a series of lanthanide complexes with POSS modified ligands. *Molecules* **2019**, *24*, 1253.

[62] Chen, M.-H.; Yoshioka, T.; Ikoma, T.; Hanagata, N.; Lin, F.-H.; Tanaka, J. Photoluminescence and doping mechanism of theranostic Eu3+/Fe3+ dual-doped hydroxyapatite nanoparticles. *Science and Technology of Advanced Materials* **2014**,

[63] Li, L.; Liu, Y.; Tao, J.; Zhang, M.; Pan, H.; Xu, X.; Tang, R. Surface modification of hydroxyapatite nanocrystallite by a small amount of terbium provides a biocompatible fluorescent probe. *The Journal of Physical Chemistry C* **2008**, *112*, 12219–12224.

[64] Lin, Y.; Yang, Z.; Cheng, J. Preparation, characterization and antibacterial property of cerium substituted hydroxyapatite nanoparticles. *Journal of rare earths* **2007**, *25*, 452–456.

[65] Phatai, P.; Futalan, C. M.; Utara, S.; Khemthong, P.; Kamonwannasit, S. Structural characterization of cerium-doped hydroxyapatite nanoparticles synthesized by an ultrasonic-assisted sol-gel technique. *Results in Physics* **2018**, *10*, 956–963.

[66] Padmanabhan, V. P.; Kulandaivelu, R.; Nellaiappan, S. N. T.; Lakshmipathy, M.; Sagadevan, S.; Johan, M. R. Facile fabrication of phase transformed cerium (IV) doped hydroxyapatite for biomedical applications–A health care approach. *Ceramics International* **2020**, *46*, 2510–2522.

[67] Singh, G.; Jolly, S. S.; Singh, R. P. Cerium substituted hydroxyapatite mesoporous nanorods: Synthesis and characterization for drug delivery applications. *Materials Today: Proceedings* **2020**, *28*, 1460–1466.

[68] Paduraru, A. V.; Musuc, A. M.; Oprea, O. C.; Trusca, R.; Iordache, F.; Vasile, B. S.; Andronescu, E. Synthesis and Characterization of Photoluminescent Ce (III) and Ce (IV) Substituted Hydroxyapatite Nanomaterials by Co-Precipitation Method: Cytotoxicity and Biocompatibility Evaluation. *Nanomaterials* **2021**, *11*, 1911.

[69] Xie, Y.; He, W.; Li, F.; Perera, T. S. H.; Gan, L.; Han, Y.; Wang, X.; Li, S.; Dai, H. Luminescence enhanced Eu3+/Gd3+ co-doped hydroxyapatite nanocrystals as imaging agents in vitro and in vivo. *ACS Applied Materials & Interfaces* **2016**, *8*, 10212–10219.

[70] Aoki, T. Photoluminescence spectroscopy. *Characterization of Materials* **2002**, 1–12.

[71] Toney, J. *"Photoluminescence Spectroscopy" in Characterization of Materials*; Spire Corporation, 2002.

[72] Asher, S. A. UV resonance Raman spectroscopy for analytical, physical, and biophysical chemistry. *Analytical chemistry* **1993**, *65*, 201A–210A.

[73] Haynes, C. L.; McFarland, A. D.; Van Duyne, R. P. Surface-enhanced Raman spectroscopy. 2005.

[74] Reimer, L. Scanning electron microscopy: physics of image formation and microanalysis. 2000.

[75] Nasrazadani, S.; Hassani, S. Modern analytical techniques in failure analysis of aerospace, chemical, and oil and gas industries. *Handbook of Materials Failure Analysis with Case Studies from the Oil and Gas Industry* **2016**, 39–54.

[76] Goldstein, J. I.; Newbury, D. E.; Michael, J. R.; Ritchie, N. W.; Scott, J. H. J.; Joy, D. C. *Scanning electron microscopy and X-ray microanalysis*; Springer, 2017.

[77] Chauhan, A.; Chauhan, P. Powder XRD technique and its applications in science and technology. *J Anal Bioanal Tech* **2014**, *5*, 1–5.

[78] Akash, M. S. H.; Rehman, K. *Essentials of Pharmaceutical Analysis*; Springer, 2020; pp 29–56.

[79] Pankove, J. I. *Optical processes in semiconductors*; Courier Corporation, 1975.

[80] Wolf, D. E. Fundamentals of fluorescence and fluorescence microscopy. *Methods in cell biology* **2007**, *81*, 63–91.

[81] Yadav, A.; Kapoor, N.; Badiye, A. Introduction to Fluorescence Microscope. *Forensic Microscopy: Truth Under the Lenses* **2022**,

[82] Koutsopoulos, S. Synthesis and characterization of hydroxyapatite crystals: a review study on the analytical methods. *Journal of Biomedical Materials Research: An Official Journal of The Society for Biomaterials, The Japanese Society for Biomaterials, and The Australian Society for Biomaterials and the Korean Society for Biomaterials* **2002**, *62*, 600–612.

[83] Lak, A.; Mazloumi, M.; Mohajerani, M. S.; Zanganeh, S.; Shayegh, M. R.; Kajbafvala, A.; Arami, H.; Sadrnezhaad, S. K. Rapid formation of mono-dispersed hydroxyapatite nanorods with narrow-size distribution via microwave irradiation. *Journal of the American Ceramic Society* **2008**, *91*, 3580–3584.

[84] Shanthi, P. M. S.; Ashok, M.; Balasubramanian, T.; Riyasdeen, A.; Akbarsha, M. Synthesis and characterization of nano-hydroxyapatite at ambient temperature using cationic surfactant. *Materials Letters* **2009**, *63*, 2123–2125.

[85] Priyadarshini, B.; Anjaneyulu, U.; Vijayalakshmi, U. Preparation and characterization of sol-gel derived Ce4+ doped hydroxyapatite and its in vitro biological evaluations for orthopedic applications. *Materials and Design* **2017**, *119*, 446–455.

[86] Murugan, R.; Ramakrishna, S. Production of ultra-fine bioresorbable carbonated hydroxyapatite. *Acta Biomaterialia* **2006**, *2*, 201–206.

[87] Serret, A.; Cabanas, M. V.; Vallet-Regi, M. Stabilization of calcium oxyapatites with lanthanum (III)-created anionic vacancies. *Chemistry of Materials* **2000**, *12*, 3836–3841.

[88] Chen, J.; Liu, J.; Deng, H.; Yao, S.; Wang, Y. Regulatory synthesis and characterization of hydroxyapatite nanocrystals by a microwave-assisted hydrothermal method. *Ceramics International* **2020**, *46*, 2185–2193.

[89] Kubelka, P.; Munk, F. An article on optics of paint layers. *Z. Tech. Phys* **1931**, *12*, 259–274.

[90] Tauc, J.; Grigorovici, R.; Vancu, A. Optical properties and electronic structure of amorphous germanium. *physica status solidi (b)* **1966**, *15*, 627–637.

[91] Rosenman, G.; Aronov, D.; Oster, L.; Haddad, J.; Mezinskis, G.; Pavlovska, I.; Chaikina, M.; Karlov, A. Photoluminescence and surface photovoltage spectroscopy studies of hydroxyapatite nano-bio-ceramics. *Journal of luminescence* **2007**, *122*, 936–938.

[92] Tsukada, M.; Wakamura, M.; Yoshida, N.; Watanabe, T. Band gap and photocatalytic properties of Ti-substituted hydroxyapatite: Comparison with anatase-TiO2. *Journal of Molecular Catalysis A: Chemical* **2011**, *338*, 18–23.

[93] Inerbaev, T. M.; Karakoti, A. S.; Kuchibhatla, S. V.; Kumar, A.; Masunov, A. E.; Seal, S. Aqueous medium induced optical transitions in cerium oxide nanoparticles. *Physical Chemistry Chemical Physics* **2015**, *17*, 6217–6221.

[94] Bazhukova, I.; Sokovnin, S. Y.; Ilves, V.; Myshkina, A.; Vazirov, R.; Pizurova, N.; Kasyanova, V. Luminescence and optical properties of cerium oxide nanoparticles. *Optical Materials* **2019**, *92*, 136–142.

[95] El-Fiqi, A.; Allam, R.; Kim, H.-W. Antioxidant cerium ions-containing mesoporous bioactive glass ultrasmall nanoparticles: Structural, physico-chemical, catalase-mimic and biological properties. *Colloids and Surfaces B: Biointerfaces* **2021**, *206*, 111932.

[96] Nelson, B. C.; Johnson, M. E.; Walker, M. L.; Riley, K. R.; Sims, C. M. Antioxidant cerium oxide nanoparticles in biology and medicine. *Antioxidants* **2016**, *5*, 15.

[97] Li, X.; Qi, M.; Sun, X.; Weir, M. D.; Tay, F. R.; Oates, T. W.; Dong, B.; Zhou, Y.; Wang, L.; Xu, H. H. Surface treatments on titanium implants via nanostructured ceria for antibacterial and anti-inflammatory capabilities. *Acta biomaterialia* **2019**, *94*, 627–643.

[98] Kurtuldu, F.; Kaňková, H.; Beltrán, A. M.; Liverani, L.; Galusek, D.; Boccaccini, A. R. Anti-inflammatory and antibacterial activities of cerium-containing mesoporous bioactive glass nanoparticles for drug-free biomedical applications. *Materials Today Bio* **2021**, *12*, 100150.

[99] Qi, M.; Li, W.; Zheng, X.; Li, X.; Sun, Y.; Wang, Y.; Li, C.; Wang, L. Cerium and its oxidant-based nanomaterials for antibacterial applications: a state-of-the-art review. *Frontiers in Materials* **2020**, *7*, 213.

[100] Wang, Z.; Tian, S.; Shao, B.; Li, S.; Li, L.; Yang, J. Cerium triflate as superoxide radical scavenger to improve cycle life of LiO2 battery. *Journal of Power Sources* **2019**, *414*, 327–332.

[101] Kanchana, P.; Navaneethan, M.; Sekar, C. Fabrication of Ce doped hydroxyapatite nanoparticles based non-enzymatic electrochemical sensor for the simultaneous determination of norepinephrine, uric acid and tyrosine. *Materials Science and Engineering: B* **2017**, *226*, 132–140.

[102] Alshahrani, A. A.; Alorabi, A. Q.; Hassan, M. S.; Amna, T.; Azizi, M. Chitosan-functionalized hydroxyapatite-cerium oxide heterostructure: an efficient adsorbent for dyes removal and antimicrobial agent. *Nanomaterials* **2022**, *12*, 2713.

[103] Bargan, A.; Ciobanu, G.; Malutan, T.; Luca, C. Influence of cerium (IV) and bismuth (III) on the luminescence properties of the nanocrystalline hydroxyapatite. *Rev. Chim.(Bucharest)* **2015**, *66*, 1910–1913.